The Astrophysical Journal Supplement Series, 257:13 (22pp), 2021 November https://doi.org/10.3847/1538-4365/ac143c

Molecules with ALMA at Planet-forming Scales (MAPS). XIII. HCO^+ and Disk Ionization Structure

Yuri Aikawa[1], Gianni Cataldi[1,2], Yoshihide Yamato[1], Ke Zhang[3,4,23], Alice S. Booth[5,6], Kenji Furuya[2], Sean M. Andrews[7], Jaehan Bae[8,9,24], Edwin A. Bergin[4], Jennifer B. Bergner[10,24], Arthur D. Bosman[4], L. Ilsedore Cleeves[11], Ian Czekala[12,13,14,15,16,24], Viviana V. Guzmán[17], Jane Huang[4,7,24], John D. Ilee[6], Charles J. Law[7], Romane Le Gal[7,18,19,20], Ryan A. Loomis[21], François Ménard[18], Hideko Nomura[2], Karin I. Öberg[7], Chunhua Qi[7], Kamber R. Schwarz[22,24], Richard Teague[7], Takashi Tsukagoshi[2], Catherine Walsh[6], and David J. Wilner[7]

[1] Department of Astronomy, Graduate School of Science, University of Tokyo, Tokyo 113-0033, Japan; aikawa@astron.s.u-tokyo.ac.jp
[2] National Astronomical Observatory of Japan, 2-21-1 Osawa, Mitaka, Tokyo 181-8588, Japan
[3] Department of Astronomy, University of Wisconsin−Madison, 475 N. Charter St., Madison, WI 53706, USA
[4] Department of Astronomy, University of Michigan, 323 West Hall, 1085 S. University Avenue, Ann Arbor, MI 48109, USA
[5] Leiden Observatory, Leiden University, 2300 RA Leiden, The Netherlands
[6] School of Physics and Astronomy, University of Leeds, Leeds LS2 9JT, UK
[7] Center for Astrophysics | Harvard & Smithsonian, 60 Garden St., Cambridge, MA 02138, USA
[8] Earth and Planets Laboratory, Carnegie Institution for Science, 5241 Broad Branch Road NW, Washington, DC 20015, USA
[9] Department of Astronomy, University of Florida, Gainesville, FL 32611, USA
[10] University of Chicago, Department of the Geophysical Sciences, Chicago, IL 60637, USA
[11] Department of Astronomy, University of Virginia, Charlottesville, VA 22904, USA
[12] Department of Astronomy and Astrophysics, 525 Davey Laboratory, The Pennsylvania State University, University Park, PA 16802, USA
[13] Center for Exoplanets and Habitable Worlds, 525 Davey Laboratory, The Pennsylvania State University, University Park, PA 16802, USA
[14] Center for Astrostatistics, 525 Davey Laboratory, The Pennsylvania State University, University Park, PA 16802, USA
[15] Institute for Computational & Data Sciences, The Pennsylvania State University, University Park, PA 16802, USA
[16] Department of Astronomy, 501 Campbell Hall, University of California, Berkeley, CA 94720-3411, USA
[17] Instituto de Astrofísica, Pontificia Universidad Católica de Chile, Av. Vicuña Mackenna 4860, 7820436 Macul, Santiago, Chile
[18] Univ. Grenoble Alpes, CNRS, IPAG, F-38000 Grenoble, France
[19] IRAP, Université de Toulouse, CNRS, CNES, UT3, 31400 Toulouse, France
[20] IRAM, 300 rue de la piscine, F-38406 Saint-Martin d'Héres, France
[21] National Radio Astronomy Observatory, 520 Edgemont Rd., Charlottesville, VA 22903, USA
[22] Lunar and Planetary Laboratory, University of Arizona, 1629 E. University Blvd., Tucson, AZ 85721, USA
Received 2021 March 3; revised 2021 June 15; accepted 2021 June 17; published 2021 November 3

Abstract

We observed HCO^+ $J = 1 - 0$ and $H^{13}CO^+$ $J = 1 - 0$ emission toward the five protoplanetary disks around IM Lup, GM Aur, AS 209, HD 163296, and MWC 480 as part of the MAPS project. HCO^+ is detected and mapped at $0\farcs3$ resolution in all five disks, while $H^{13}CO^+$ is detected ($S/N > 6\sigma$) toward GM Aur and HD 163296 and tentatively detected ($S/N > 3\sigma$) toward the other disks by a matched filter analysis. Inside a radius of $R \sim 100$ au, the HCO^+ column density is flat or shows a central dip. At outer radii ($\gtrsim$100 au), the HCO^+ column density decreases outward, while the column density ratio of HCO^+/CO is mostly in the range of $\sim 10^{-5}$–10^{-4}. We derived the HCO^+ abundance in the warm CO-rich layer, where HCO^+ is expected to be the dominant molecular ion. At $R \gtrsim 100$ au, the HCO^+ abundance is $\sim 3 \times 10^{-11} - 3 \times 10^{-10}$, which is consistent with a template disk model with X-ray ionization. At the smaller radii, the abundance decreases inward, which indicates that the ionization degree is lower in denser gas, especially inside the CO snow line, where the CO-rich layer is in the midplane. Comparison of template disk models with the column densities of HCO^+, N_2H^+, and N_2D^+ indicates that the midplane ionization rate is $\gtrsim 10^{-18}$ s^{-1} for the disks around IM Lup, AS 209, and HD 163296. We also find hints of an increased HCO^+ abundance around the location of dust continuum gaps in AS 209, HD 163296, and MWC 480. This paper is part of the MAPS special issue of the Astrophysical Journal Supplement.

Unified Astronomy Thesaurus concepts: Astrochemistry (75); Planetary system formation (1257); Protoplanetary disks (1300)

Supporting material: figure set

1. Introduction

Protoplanetary disks are the birth site of planetary systems, including our solar system. The rate and degree of ionization are important parameters for both the physical and chemical evolution of the disk, and thus for the formation of planetary systems. The disk gas is much denser, and thus its ionization degree x_i, which is the relative abundance of electrons to H_2, is much lower than in parental molecular clouds (e.g., Umebayashi & Nakano 1988).[25] Yet the ionization degree is expected to be sufficient for the gas to be partially coupled with the magnetic fields present in the disk, which could induce magnetohydrodynamic instabilities, disk winds, and thus the

[23] NASA Hubble Fellow.
[24] NASA Hubble Fellowship Program Sagan Fellow.

[25] Considering neutrality, the electron abundance should be the same as the total abundance of cations. In dense midplane regions, grain particles can be the dominant charge carrier.

angular momentum transfer needed for mass accretion (e.g., Suzuki & Inutsuka 2009; Bai & Stone 2013). More specifically, the ionization degree, and thus the coupling between gas and magnetic fields (i.e., nonideal MHD effects), should vary spatially within the disk, which affects the physical structure of the disk (e.g., Béthune et al. 2017). Ionization also triggers ion−molecule reactions in the disk. For example, carbon monoxide, which is the main tracer of disk gas, can be converted to other species by ion−molecule reactions within the typical evolutionary timescale of the disk (10^6 yr), if the ionization rate ζ is similar to or higher than the cosmic-ray (CR) ionization rate in the interstellar medium (10^{-17} s^{-1}; Bergin et al. 2014; Furuya & Aikawa 2014; Bosman et al. 2018; Schwarz et al. 2018).

The ionization degree is determined by the ionization rate, gas density, and number density and size distribution of dust grains. For protoplanetary disks, there are several possible ionization sources: X-rays from the central star, CRs and stellar energetic particles, and the decay of short-lived radio active nuclei (SLRs) (e.g., Umebayashi & Nakano 1981; Glassgold et al. 1997; Umebayashi & Nakano 2009; Rab et al. 2017). X-rays are the dominant ionization source in the disk surface. However, X-rays are significantly attenuated before reaching the disk midplane. The attenuation length corresponds to a hydrogen column density of $N_{\rm H} \sim 10^{22}$ cm^{-2} at 1 keV, while the hydrogen column densities of our target disks are $\sim 10^{23}$–10^{25} cm^{-2} at the radius of 100 au (Zhang et al. 2021). Although the attenuation length is larger at higher energies, the X-ray ionization rate is still expected to be $\lesssim 10^{-18}$ s^{-1} in the midplane (e.g., Section 4; see also Rab et al. 2018). The CR ionization rate is $\sim 5 \times 10^{-17}$ s^{-1} in molecular clouds (Dalgarno 2006), and its attenuation length is much larger than that of X-rays. While Umebayashi & Nakano (1981) evaluated the attenuation length to be 96 g cm^{-2}, more recent work by Padovani et al. (2018) reassessed the propagation of CR particles and obtained an even larger attenuation length. But CRs can be scattered by magnetized stellar winds and/or magnetic fields in the disk (e.g., Umebayashi & Nakano 1981; Cleeves et al. 2014; Padovani et al. 2018). Stellar energetic particles could also be disturbed by magnetic fields. Finally, the ionization rate from the decay of ^{26}Al is estimated to be 10^{-18} s^{-1} in the primordial solar system based on meteorite analysis (e.g., Umebayashi & Nakano 2009). While the abundance of SLRs should vary among star-forming regions, recent chemo-hydrodynamic simulations of the Milky Way predict that the abundance of ^{26}Al in the primordial solar system may be typical for other star-forming regions (Fujimoto et al. 2018). In summary, the dominant ionization source and ionization degree should vary spatially within the disk and could be different between disks.

The importance of understanding ionization processes motivates the observation of molecular ions in protoplanetary disks. Theoretical models show that the major molecular ions in disks are H_3^+, HCO^+, N_2H^+, and their deuterated isotopologues (e.g., Aikawa & Herbst 2001; Bergin et al. 2007; Willacy 2007; Aikawa et al. 2015, 2018). The most abundant molecular ion varies both radially and vertically in disks (Figure 1). The disk surface is the photon-dominated region (PDR); photoionization makes atomic ions such as C^+ and S^+ the main charge carriers. Deeper in the disk, H_3^+ becomes the most abundant ion, while HCO^+ becomes dominant when the abundance ratio n(CO)/n(e) is higher than $\sim 10^3$, where $n(i)$ denotes the number density of species i (Aikawa et al. 2015). In the regions where $T < 20$ K (i.e., below the CO snow surface and outside the CO snow line), CO freezes out onto grains, which enhances the N_2H^+ abundance. As temperature

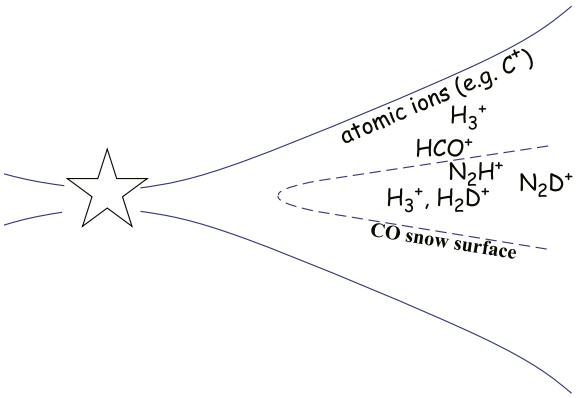

Figure 1. Schematic distribution of major ions in protoplanetary disks.

declines toward deeper layers, the dominant ion changes from N_2H^+ to H_3^+ and its deuterated isotopologues. Unfortunately, H_3^+ cannot be observed at millimeter wavelengths, and its deuterated isotopologues have not been detected in disks so far. N_2D^+ is considered to be an alternative probe to constrain the ionization degree in the cold midplane (Cleeves et al. 2014).

While the rotational transitions of HCO^+, N_2H^+, and their isotopologues have been observed toward several disks, a quantitative evaluation of their column densities and the disk ionization degree has been reported only in a limited number of references. Öberg et al. (2011b) used the IRAM 30 m telescope to observe $H^{13}CO^+$ $J = 3 - 2$ in the disk of DM Tau. They combined their observation with previous Submillimeter Array (SMA) data of N_2H^+ $J = 3 - 2$, HCO^+ $J = 3 - 2$, and DCO^+ $J = 3 - 2$ to estimate the ionization degree in three temperature regions of the disk: in the upper warm molecular layer ($T > 20$ K), the ionization degree $x_{\rm i}$ is estimated to be 4×10^{-10} based on the HCO^+ data. In the cooler molecular layer ($T = 16$–20 K), where N_2H^+ and DCO^+ would be abundant, $x_{\rm i}$ is derived to be 3×10^{-11}, while in the cold, dense midplane ($T < 16$ K), the nondetection of H_2D^+ constrains $x_{\rm i}$ to be $< 3 \times 10^{-10}$. Teague et al. (2015) observed HCO^+ $J = 1 - 0$ and $J = 3 - 2$ and DCO^+ $J = 3 - 2$ in DM Tau at $\sim 1\farcs5$ resolution using the Plateau de Bure Interferometer. The column densities of HCO^+ and DCO^+ at a radius of 100 au are derived to be 9.8×10^{12} cm^{-2} and 1.2×10^{12} cm^{-2}, respectively. They derive an ionization degree of $\sim 10^{-7}$ from the abundance ratio of DCO^+/HCO^+, assuming steady-state balance between $H_3^+ + HD \rightarrow H_2D^+ + H_2$, $H_2D^+ + CO \rightarrow DCO^+ + H_2$, and the destruction of DCO^+ (Caselli et al. 2002). Cleeves et al. (2015) calculated chemical models of the disk around TW Hya for various CR ionization rates $\zeta_{\rm CR}$ and X-ray spectra. Instead of evaluating molecular column densities from the observational data, they calculated the disk-integrated flux of molecular lines from the models to compare with their own HCO^+ and $H^{13}CO^+$ $J = 3 - 2$ observations of TW Hya and HCO^+, $H^{13}CO^+$, and N_2H^+ data from the literature (e.g., Qi et al. 2013a, 2013b). They concluded that the observations are best reproduced by the model with low CR ionization rate $\zeta_{\rm CR} \lesssim 10^{-19}$ s^{-1} and modest X-ray spectra, in which the ionization degree is $\sim 10^{-11}$–10^{-10} near the midplane outside of a radius of $\sim$100 au. Since the ionization degree varies spatially and between disks, observations with higher spatial resolution and toward more targets are highly desirable.

In light of the ring−gap structures observed in the millimeter dust continuum of many disks in recent years

(e.g., Andrews et al. 2018; Huang et al. 2018; Cieza et al. 2021), it is also interesting to investigate whether and how the molecular ion abundances and ionization degree correlate with the dust substructures. Theoretical studies predict that HCO^+ is sensitive to, and thus could be a good probe of, gas density and/or small dust abundance. In the region where HCO^+ is the most abundant positive charge carrier, its abundance (i.e., ionization degree) should be proportional to $n_H^{-1/2}$ (e.g., Duley & Williams 1984). In the gap region, the ionization degree could also be enhanced owing to deeper penetration of X-rays. Aikawa & Nomura (2006), on the other hand, showed that the HCO^+ column density declines as the abundance of sub-micron-sized dust grains decreases with grain growth. This is because the PDR, in which atomic ions dominate over molecular ions, extends deeper into the disk when the abundance of submicron dust grains decreases. Similar results are obtained in models of disks around Herbig Ae stars (Jonkheid et al. 2007; see also Wakelam et al. 2019). While these models do not include any ring−gap structures, they indicate that the HCO^+ abundance could vary over the substructures. The HCO^+ abundance would be higher in the gap than in the ring, if the gas density is lower but the UV attenuation is sufficient in the gap. On the other hand, the HCO^+ abundance would be lower in the gap if the UV penetration is significant (see also Smirnov-Pinchukov et al. 2020).

In the present work, we analyze the $J = 1 - 0$ transition of HCO^+ and $H^{13}CO^+$ toward five disks around IM Lup, GM Aur, AS 209, HD 163296, and MWC 480 observed as a part of the Molecules with ALMA at Planet-forming Scales (MAPS) Large Program (Öberg et al. 2021, project code 2018.1.01055.L). For a given column density of HCO^+ at a lukewarm temperature (a few tens of kelvin), which corresponds to the CO-rich molecular layer in the disk, the $J = 1 - 0$ line tends to be optically thinner than higher transitions and thus useful to derive the column density. Our spatial resolution, 0.″3, is high enough to investigate the radial distribution of HCO^+ and to marginally resolve the continuum gap regions. We also combine our results with the analysis of CO isotopologues, N_2H^+, and N_2D^+ in the companion MAPS papers by Zhang et al. (2021) and Cataldi et al. (2021) to estimate the radial variation in the ionization degree and the ionization rate in the disks. Various data products of the MAPS project, including the present work, such as reduced observational data, zeroth-moment maps, as well as derived HCO^+ column densities can be downloaded at www.alma-maps.info.

The outline of this paper is as follows. We briefly describe the observations in Section 2. Section 3 describes the observational results: the zeroth-moment maps, radial emission profiles, azimuthally averaged spectra, and molecular column densities. We derive the HCO^+ abundance, which corresponds to a lower limit of the ionization degree in the warm molecular layer, and compare our results with a template disk chemistry model in Section 4. Our conclusions are presented in Section 5.

2. Observations

The observational setup chosen by MAPS covered four spectral setups: two in Band 3 at ∼3 mm and two in Band 6 at ∼1 mm. The $J = 1 - 0$ transitions of HCO^+ and $H^{13}CO^+$ are in one of the Band 3 setups. The spectral resolution is 0.237 km s^{-1} for HCO^+ and 0.488 km s^{-1} for $H^{13}CO^+$. Molecular data for the targeted lines are taken from the CDMS database[26] (Müller et al. 2001; Endres et al. 2016) and summarized in Table 1.

[26] https://cdms.astro.uni-koeln.de/

Table 1
Molecular Data of the Targeted Lines Taken from the CDMS Database

Transition	FRequency (GHz)	A_{ij}[a] (s^{-1})	E_u[b] (K)
HCO^+ $J = 1 - 0$	89.1885247	4.2512×10^{-5}	4.28
$H^{13}CO^+$ $J = 1 - 0$	86.7542884	3.8534×10^{-5}	4.16

Notes.
[a] Einstein A-coefficient.
[b] Upper-state energy.

Two array configurations were used: a short-baseline configuration that was sensitive to extended structure, and a long-baseline configuration to achieve high angular resolution. The details of the data calibration are described in Öberg et al. (2021). The MAPS collaboration produced images from the calibrated visibilities using the CLEAN algorithm implemented in the CASA `tclean` task. Details of the imaging procedure are described in Czekala et al. (2021). We use the fiducial images provided by MAPS, which have a 0.″3 circular beam. This beam size corresponds to a physical size of 30.3 au at the distance of HD 163296, which is the closest target, and 48.6 au at the distance of MWC 480, which is the most distant. Basic properties of the data cubes such as noise levels are summarized in Tables 11 and 12 in Öberg et al. (2021).

3. Observational Results

3.1. Zeroth-moment Maps, Disk-integrated Fluxes, and Radial Emission Profiles

The MAPS collaboration produced zeroth-moment maps by applying a Keplerian mask to the data cubes and integrating over the velocity axis (Law et al. 2021a). The mask parameters are conservatively chosen to incorporate all ^{13}CO $J = 2 - 1$ emission, which is the most widespread emission of any species except for CO $J = 2 - 1$. The mask parameters for the five disk are summarized in Table 1 in Czekala et al. (2021). The stellar masses adopted for the generation of the masks are listed in Table 1 in Öberg et al. (2021). These maps were used for all scientific analysis, in particular to derive radial emission profiles (Law et al. 2021a). A Keplerian mask, however, introduces spatial variance in noise distribution, since the number of channels summed to create the zeroth-moment maps varies spatially. The discontinuous noise distribution occasionally causes arc-like artifacts, which could be mistaken as real substructure, in the central regions. To mitigate such artifacts, MAPS also produced "hybrid" zeroth-moment maps by combining a Keplerian mask and a smoothed σ-clip mask (thus their name "hybrid"; see Law et al. 2021a, Appendix A). The latter removes the pixels with an S/N below a given threshold. We emphasize that by using a clipping mask with a threshold larger than 0σ, some emission is inevitably lost. Therefore, the hybrid zeroth-moment maps are for presentational purposes only and are not used for any quantitative analysis.

In Figure 2, we show hybrid zeroth-moment maps for HCO^+ $J = 1 - 0$ and $H^{13}CO^+$ $J = 1 - 0$. We choose the best-looking σ-clip value by visual inspection: 1σ for HCO^+ $J = 1 - 0$ toward IM Lup, and 0σ for the other maps. Hybrid zeroth-moment maps with a 0.″5 tapered beam are shown in Figure 13 in Appendix A; the faint emission is more easily seen in the lower spatial resolution images.

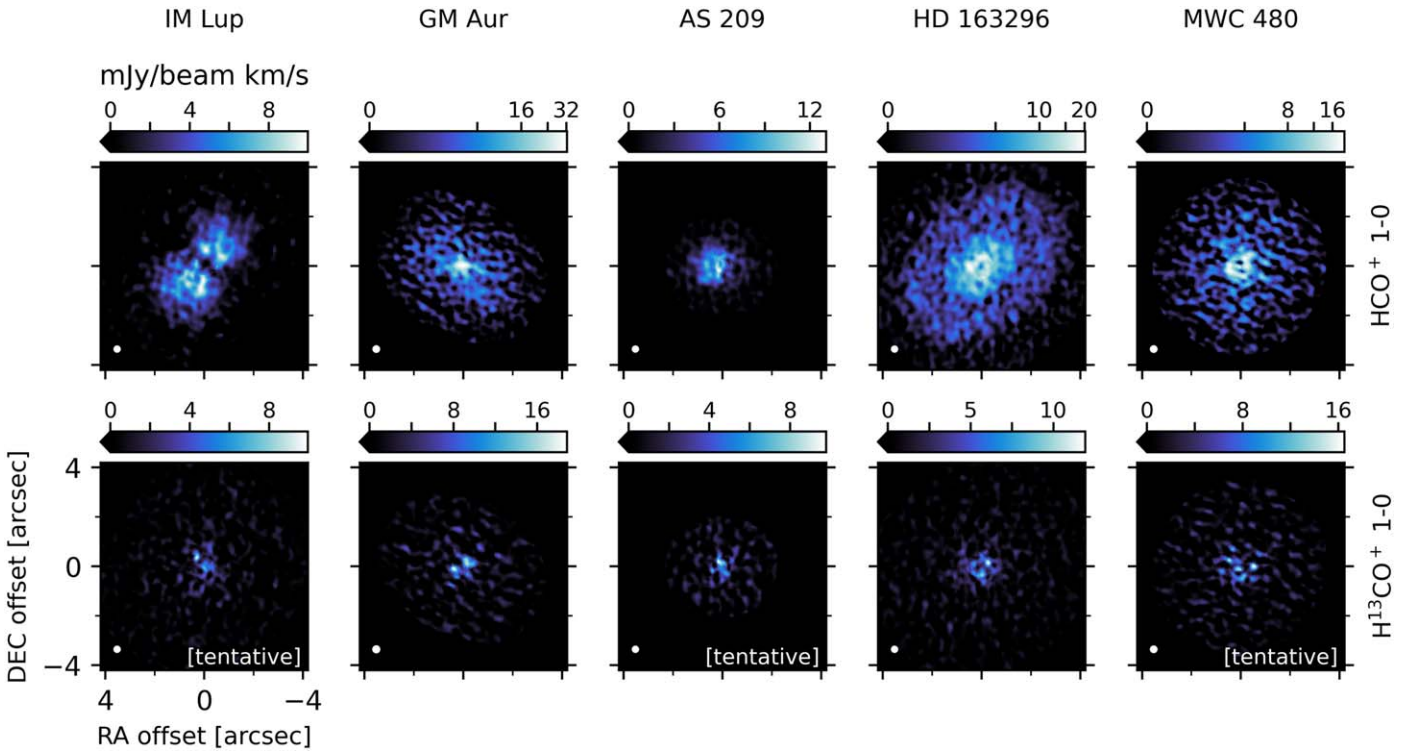

Figure 2. Gallery of hybrid zeroth-moment maps for HCO^+ $J = 1 - 0$ (top row) and $H^{13}CO^+$ $J = 1 - 0$ (bottom row) for the MAPS sample, ordered from left to right by increasing stellar mass (see Table 1 in Öberg et al. 2021). These maps were generated by combining a Keplerian mask with a smoothed σ-clip mask (Appendix A of Law et al. 2021a). The color scales employ either linear or arcsinh stretches, with the lower end saturating at 0 mJy beam^{-1} km s^{-1}. The synthesized beam is shown by the white ellipse in the lower left corner of each panel. Due to the use of a mask, the noise level is not constant across a map. Lines that are only tentatively detected in total flux or matched filter are marked in the lower right corner of the panel.

Table 2
Disk-Integrated Fluxes

	HCO^+ 1–0			$H^{13}CO^+$ 1–0[a]			$H^{13}CO^+$ 1–0[b]		
	r_{min}[c] (au)	r_{max}[d] (au)	Flux (mJy km s^{-1})	r_{min} (au)	r_{max} (au)	Flux (mJy km s^{-1})	r_{min} (au)	r_{max} (au)	Flux (mJy km s^{-1})
IM Lup	0	700	519 ± 53	0	700	<46	0	400	23 ± 6
GM Aur	0	500	412 ± 42	0	500	<43	0	400	27 ± 7
AS 209	0	300	178 ± 19	0	300	<33	0	200	<26
HD 163296	0	550	1002 ± 101	0	550	<54	50	400	27 ± 7
MWC 480	0	550	323 ± 34	0	550	<34	50	100	<18

Notes. Upper limits are at 3σ significance.
[a] For a Keplerian mask with the same radial extent as used for HCO^+ 1–0.
[b] For a Keplerian mask with the same radial extent as the matched filter that maximizes the S/N of the filter response (see Appendix B and Figure 14).
[c] Minimum radius of the Keplerian mask.
[d] Maximum radius of the Keplerian mask.

The HCO^+ $J = 1 - 0$ line is clearly detected in all five disks. The emission is relatively bright inside a radius of ~200 au, while its diffuse emission extends to $\gtrsim$400 au, except for the disk of AS 209, in which the emission extends only up to $R \sim 300$ au. In AS 209, the emission from the west side of the disk is absorbed by a foreground cloud, which happens to have a similar line-of-sight velocity (Öberg et al. 2011a). We thus performed all analysis for AS 209 only on the unobscured east side of the disk within a $\pm 55°$ wedge centered on the semimajor axis (Teague et al. 2018b; Law et al. 2021a). The emission of $H^{13}CO^+$ $J = 1 - 0$ is very weak and is not clearly seen in the zeroth-moment maps.

Disk-integrated fluxes of HCO^+ $J = 1 - 0$ and $H^{13}CO^+$ $J = 1 - 0$ are presented in Table 2. These were calculated by integrating the flux within a Keplerian mask. The radial extent of the Keplerian mask is different from that used for the zeroth-moment maps. For HCO^+, the radial extent of the mask is visually determined from the extent of the emission seen in the radial emission profile (see Figure 3 and Table 2). For $H^{13}CO^+$, we measured fluxes by using the same radial extents as for HCO^+. In an attempt to increase the signal-to-noise ratio (S/N), we computed additional fluxes by adopting the same radial extent as the Keplerian models that maximize the S/N in the matched filter analysis in the *u-v* plane (Appendix B,

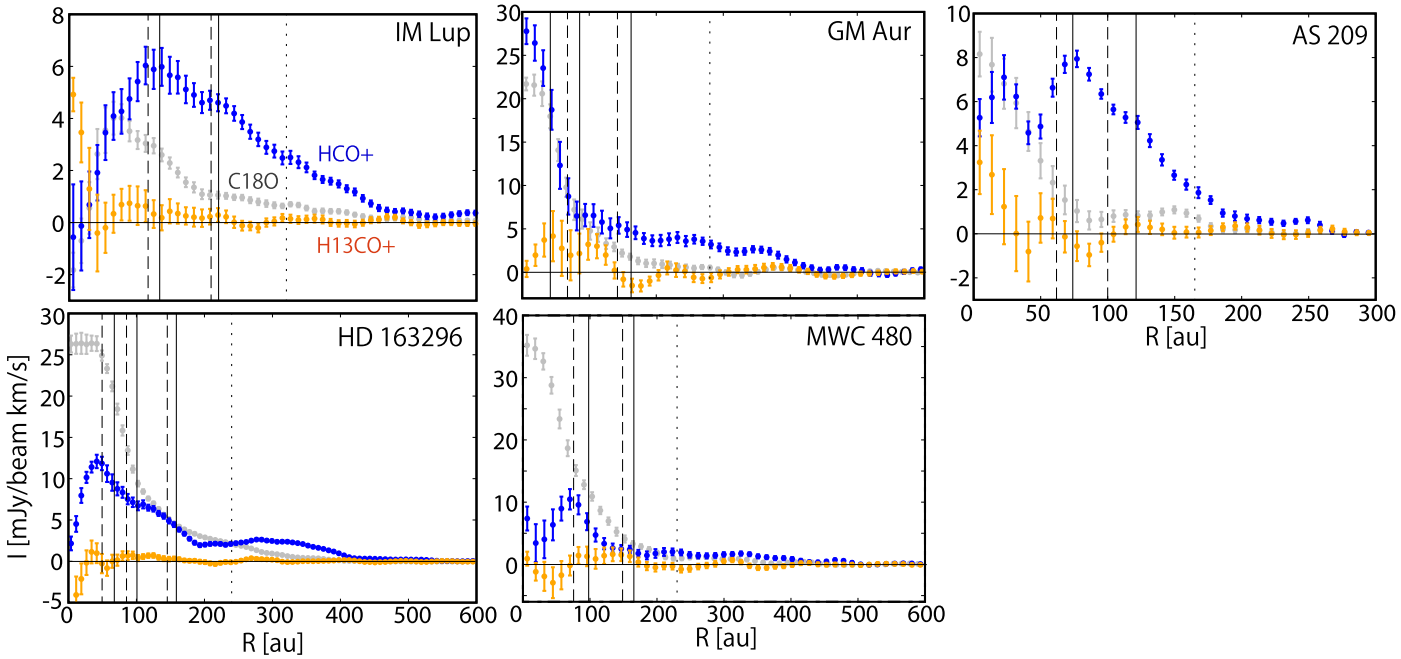

Figure 3. Radial emission profiles of HCO^+ $J = 1 - 0$, $H^{13}CO^+$ $J = 1 - 0$, and $C^{18}O$ $J = 1 - 0$ for IM Lup, GM Aur, AS 209, HD 163296, and MWC 480. The error bar shows the $\pm 1\sigma$ error. The size of the radial bins is $0\farcs075$, which is a quarter of the beam size. The vertical lines indicate the positions of rings (solid), gaps (dashed), and the edge of millimeter dust continuum (dotted) referring to Huang et al. (2018), Long et al. (2018), Liu et al. (2019), and Law et al. (2021a) (see also Sierra et al. 2021).

Figure 14), as shown in the right column of Table 2. Errors were calculated by repeating the flux measurement procedure at off-source positions and taking the standard deviation of the off-source fluxes. A 10% flux calibration error was added in quadrature. If the resulting S/N was smaller than 3, Table 2 reports the 3σ upper limit. To calculate these disk-integrated fluxes and errors, we used the image cubes that are not corrected for the primary beam. This is because for primary-beam-corrected images, the noise increases toward the edges of the image, making our approach to estimate the error from off-source positions invalid. However, we verified that the difference to fluxes extracted from primary-beam-corrected images is negligible. For deriving radially resolved column density profiles, we use the primary-beam-corrected images.

$H^{13}CO^+$ is seen with S/N > 3 for IM Lup, GM Aur, and HD 163296, if we use the masks with the extent informed by the matched filter analysis. The matched filter analysis itself (Appendix B) gives a response larger than 6σ for GM Aur and HD 163296 and larger than 3σ for the other disks. Thus, we consider $H^{13}CO^+$ $J = 1 - 0$ detected in GM Aur and HD 163296, and tentatively detected for the other three disks. We note that the values in Table 2 are different from those in Table 12 in Öberg et al. (2021), who adopted the same Keplerian masks to generate zeroth-moment maps and to estimate disk-integrated fluxes.

Figure 3 shows the radial emission profiles of the $J = 1 - 0$ transitions of HCO^+ and $H^{13}CO^+$. These profiles are produced by azimuthally averaging the zeroth-moment maps that were produced with a Keplerian mask only (i.e., without a σ-clip mask). The inclination and position angles of each disk are listed in Table 1 in Öberg et al. (2021). Since HCO^+ is expected to be formed by CO + H_3^+ and to be a dominant molecular ion in CO gas-rich layers, we also plotted the radial emission profile of $C^{18}O$ $J = 1 - 0$ derived by Law et al. (2021a). The vertical lines indicate the radius of rings (solid), gaps (dashed), and the dust disk edge (dotted) observed in the millimeter dust continuum (Huang et al. 2018; Long et al. 2018; Liu et al. 2019; Law et al. 2021a; Sierra et al. 2021). Both HCO^+ emission and $C^{18}O$ emission extend out to several hundred astronomical units. In the IM Lup disk, the radial emission profile of HCO^+ $J = 1 - 0$ is similar to that of $C^{18}O$, showing a ring-like distribution, although the peak position of the HCO^+ emission is ~36 au outside of the $C^{18}O$ peak. In GM Aur, on the other hand, both the $C^{18}O$ emission and HCO^+ emission are centrally peaked. The radial emission profiles of $C^{18}O$ and HCO^+ are quite different in AS 209: around a radius of ~77 au, the HCO^+ emission has a local maximum, while the radial gradient of $C^{18}O$ changes from negative to plateau. Interestingly, the peak position of the HCO^+ emission coincides with that of a dust continuum ring. In the disks around the Herbig Ae stars, HD 163296 and MWC 480, the HCO^+ emission shows a central dip, while $C^{18}O$ is flat for HD 163296 and centrally peaked for MWC 480.

The intensity ratio of the $C^{18}O$ and HCO^+ lines varies significantly with radius and among objects. For example, the ratio reaches ~5 toward the center of the MWC 480 disk, while HCO^+ is brighter than $C^{18}O$ around $R \sim 77$ au in AS 209. Although this indicates that the abundance (column density) ratio of HCO^+ to $C^{18}O$ also varies, we need to consider the line optical depth. Under LTE conditions with an excitation temperature of 30 K, which is a typical temperature in the warm molecular layers, the optical depth of $C^{18}O$ $J = 1 - 0$ reaches unity for a $C^{16}O$ column density of $\sim 6 \times 10^{18}$ cm^{-2}, assuming a $^{16}O/^{18}O$ isotope ratio of 557 (Wilson 1999). Zhang et al. (2021) derived the radial column density distribution of CO by analyzing several transitions of CO and its isotopologues. The CO column density exceeds 6×10^{18} cm^{-2} inside a radius of ~100 au in the GM Aur, HD 163296, and MWC 480 disks. At least for these inner radii, $C^{18}O$ $J = 1 - 0$ is optically thick, and thus the intensity ratio of $C^{18}O$ to HCO^+ does not

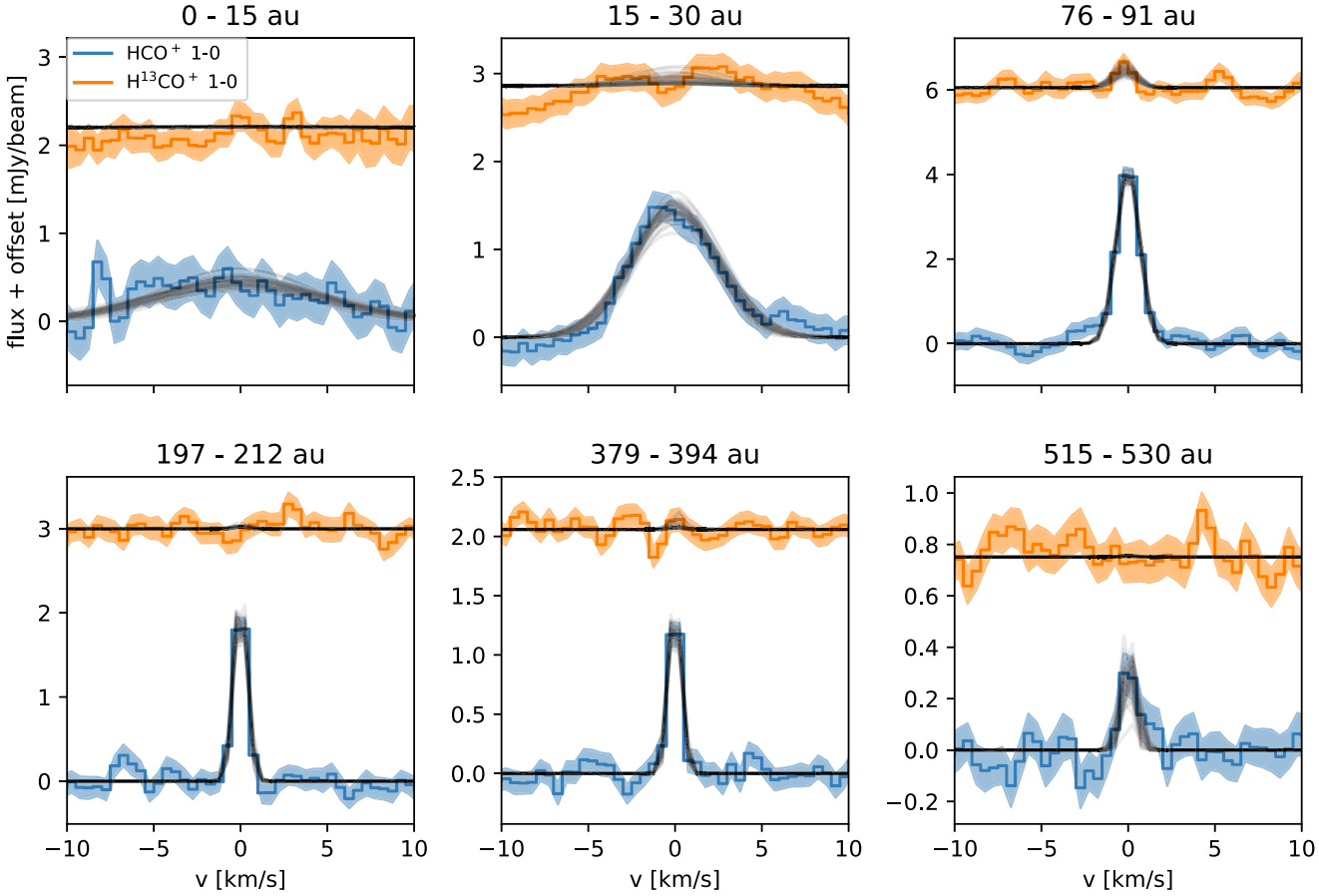

Figure 4. Examples of HCO^+ and $H^{13}CO^+$ $J = 1 - 0$ model spectra fit to azimuthally averaged spectra of HD 163296 for a few radial bins. The orange and blue solid lines show the data, with the shaded regions corresponding to the 1σ uncertainty. The black curves show 50 randomly selected models drawn from the Monte Carlo chain, with the selection probability being proportional to the posterior probability of the model. Spectra are vertically offset for clarity.

reflect their column density ratio. We also need to evaluate the optical depth of HCO^+ to derive its column density; the optical depth of HCO^+ $J = 1 - 0$ reaches unity for a HCO^+ column density of $\sim 1 \times 10^{13}$ cm^{-2} under LTE conditions at a temperature of 30 K.

3.2. Azimuthally Averaged Spectra and Radial Profiles of the HCO^+ Column Density

In order to evaluate the radial profile of the optical depth and column density of HCO^+, we first derive the azimuthally averaged spectrum for radial bins with a width of half the beam size. Due to the Keplerian rotation of the disk, at each spatial location in the data cube, the spectrum is shifted with respect to the systemic velocity. We thus shift each spectrum by the Keplerian velocity projected to the line of sight before averaging the spectra azimuthally. This results in all individual spectra being centered at the systemic velocity, which increases the S/N of the azimuthally averaged spectrum (Teague et al. 2016; Yen et al. 2016; Matrà et al. 2017). The calculation of the error bars of the averaged spectrum is described in detail in Appendix D of Cataldi et al. (2021). Briefly, we calculate both the standard deviation of the spectrum in regions without line emission and an analytical error bar based on the number of independent samples included in the average. We then adopt the maximum of the two as our final error bar. Figure 4 shows examples of extracted spectra of HD 163296. The full gallery of spectra is found in Appendix C.

Table 3
Free Parameters for Fitting of Azimuthally Averaged Spectra to Derive the HCO^+ Column Density

Parameter	Prior Low[a]	Prior High[b]	Units
$\log N_{HCO^+}$	1	16	$\log(cm^{-2})$
T_{ex}	10	100	(K)
$FWHM_{kernel}$	0.5[c]	variable[d]	(km s^{-1})
Δv_{HCO^+}[e]	−0.3	0.3	(km s^{-1})
$\Delta v_{H^{13}CO^+}$	−0.3	0.3	(km s^{-1})

Notes.
[a] Lower bound of flat prior.
[b] Upper bound of flat prior.
[c] Equal to the channel width.
[d] Initial value for innermost radial bin is 20 km s^{-1}. Dynamically adjusted when sequentially fitting larger and larger radii (see Cataldi et al. 2021, for details).
[e] Offset of the line center with respect to the systemic velocity.

We then calculate the column density of HCO^+, $N(HCO^+)$, at each radial bin by simultaneously fitting the azimuthally averaged spectra of HCO^+ and $H^{13}CO^+$. We employ the same fitting procedure as Cataldi et al. (2021). Briefly, for a given HCO^+ column density, we compute HCO^+ $J = 1 - 0$ and $H^{13}CO^+$ $J = 1 - 0$ model spectra that can be compared to the data. There are five free parameters: the logarithm of the HCO^+ column density, the excitation temperature, an offset Δv of the line center with respect to the systemic velocity for each

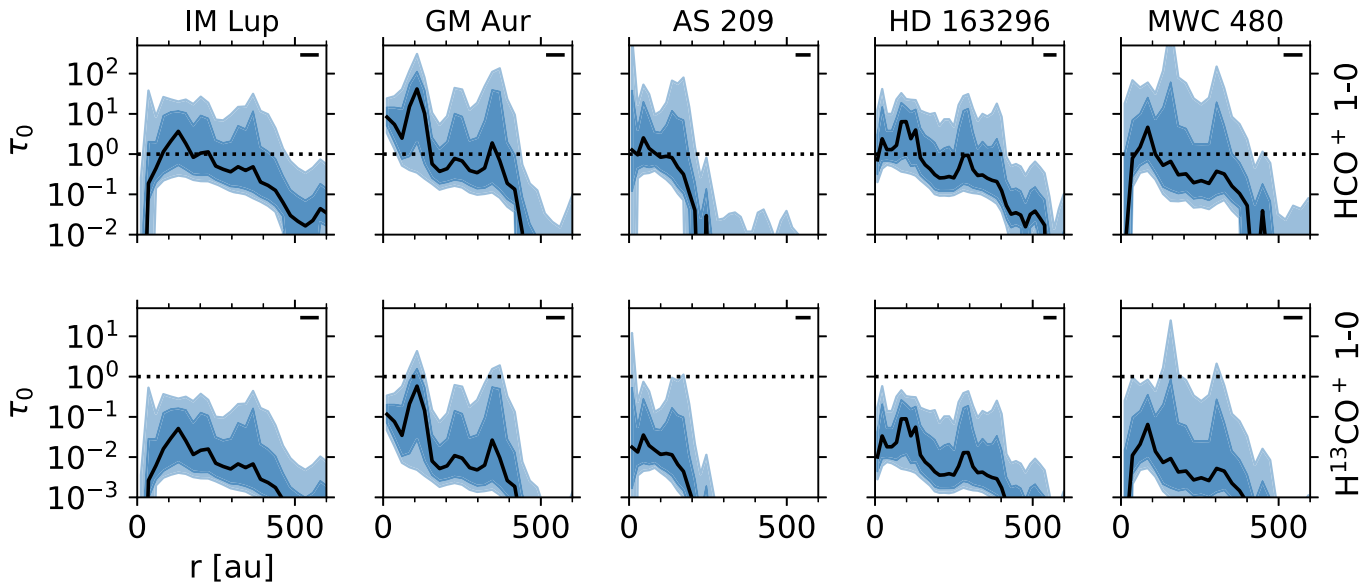

Figure 5. Optical depth profiles of HCO^+ ($J = 1 - 0$) and $H^{13}CO^+$ ($J = 1 - 0$) derived from fitting azimuthally averaged spectra. The black lines show the median of the posterior probability, while the shaded regions extend from the 16th to 84th percentile and from the 2.3th to 97.7th percentile. The beam size is shown as a horizontal line in the upper right corner.

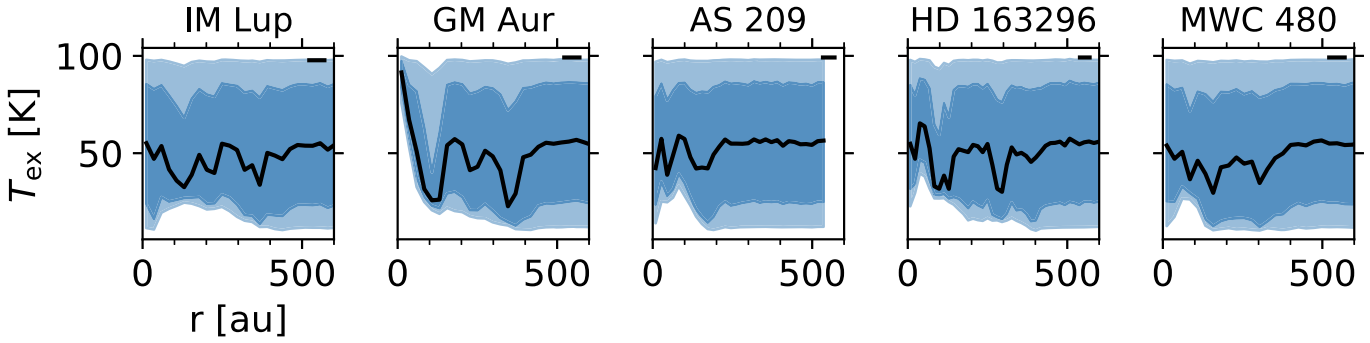

Figure 6. The excitation temperature derived from fitting azimuthally averaged spectra. The black lines show the median of the posterior probability, while the shaded regions extend from the 16th to 84th percentile and from the 2.3th to 97.7th percentile. The beam size is shown as a horizontal line in the upper right corner.

line, and the FWHM of the Gaussian kernel with which the model spectra are convolved to mimic observational broadening. The $H^{13}CO^+$ column density is fixed to 1/68 of the HCO^+ column density (Milam et al. 2005). We use a Markov Chain Monte Carlo (MCMC) method implemented in the `emcee` package (Foreman-Mackey et al. 2013) to explore the parameter space and assume flat priors. We employ 200 walkers taking 5000 steps each, and we discard the first 2500 steps from the analysis. The free parameters and the prior boundaries are listed in Table 3. The full details of the fitting procedure can be found in Cataldi et al. (2021). Figure 4 shows examples of model spectra fitted to the HD 163296 data. The full gallery of models is shown in Appendix C.

Figures 5 and 6 show the optical depths and excitation temperature derived by fitting the azimuthally averaged spectra, respectively. We find that HCO^+ $J = 1 - 0$ is optically thick at the column density peaks. However, we are still able to constrain the HCO^+ column density because the $H^{13}CO^+$ $J = 1 - 0$ transition is in the optically thin regime. The top panels in Figure 7 present the derived HCO^+ column densities.

The excitation temperature is poorly constrained for large radial regions of the disks, as shown in Figure 6. However, at least a lower limit on the excitation temperature can be placed in some disk locations. The innermost ∼50 au of GM Aur stand out with an apparently well-constrained $T_{ex} \approx 90$ K. This region also requires a large FWHM of 17 km s^{-1}. These rather extreme parameters might indicate that the fit is not reliable. In fact, considerable broadening is seen for all disks for the two innermost radial bins (i.e., within one beam FWHM from the disk center) owing to beam smearing of the large velocity gradient in the inner disk (see Figures 16). Therefore, the column density estimates for the two innermost radial bins should be considered with caution.

In Appendix D, we show optical depth and column density profiles for additional fits where the excitation temperature has been fixed to 30 K, which is a typical temperature for the warm molecular layer where HCO^+ is expected to be present. The corresponding models are shown in Figure 16. The column densities generally agree well with the fits where T_{ex} is a free parameter, as can be seen in Figure 17. Furthermore, for both fits, the model spectra fit the data well (Figure 16). One exception is the region inward of ∼150 au toward GM Aur, where the models with T_{ex} as a free parameter generally provide a better fit, especially for the two innermost

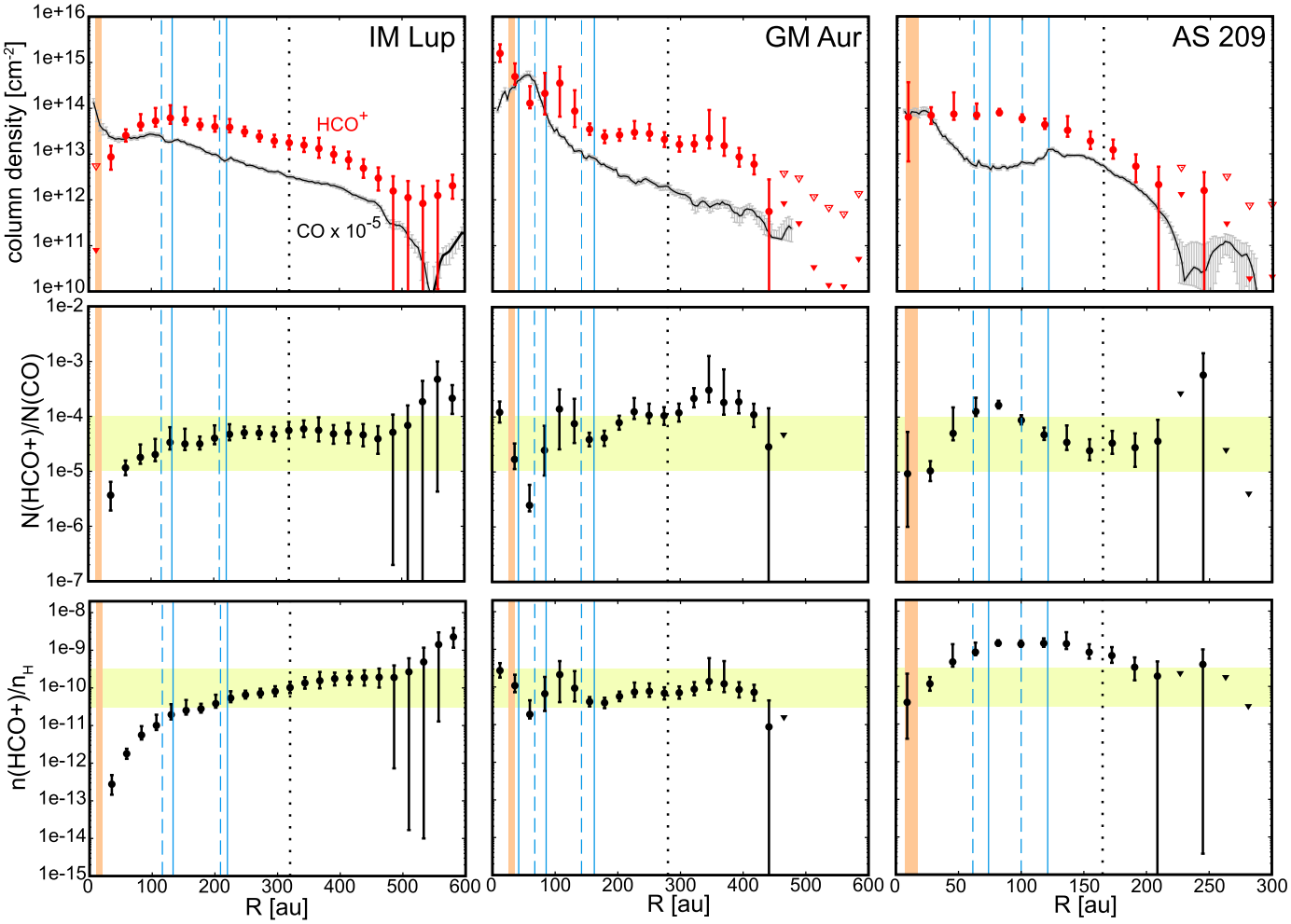

Figure 7. Top: column densities of HCO^+ (red) and CO column density scaled by 10^{-5} (black lines with gray error bars). The error bars correspond to 10% or 1σ for CO (see Section 3.2), while they show the 16th and 84th percentiles for HCO^+. At radii where the median value of the molecular column density is lower than the value at 16th percentile by a factor of >10, we plot the upper limits as inverted triangles (84th percentile for closed triangles and 98th percentile for open triangles). The vertical orange bars mark the CO snow line as inferred from the model by Zhang et al. (2021) with error of ±5 au. The blue solid and dashed lines depict the radius of rings and gaps, respectively, in dust continuum. The black dotted lines depict the outer edge of the millimeter dust continuum. Middle: the column density ratio of HCO^+ to CO. The yellow bars mark the HCO^+/CO column density ratio of $10^{-5} - 10^{-4}$. Bottom: abundance of HCO^+ relative to hydrogen nuclei in the CO gas-rich layer. The yellow bars mark the abundance of 3×10^{-11}–3×10^{-10}. In the middle and bottom panels, we consider only the error in HCO^+ column density, since it dominates over the error of CO column density estimates. At radii where the median value of the HCO^+ column density is lower than the value at 84th percentile by a factor of >10, we plot the value that corresponds to the 1σ upper limit (i.e., 84th percentile of HCO^+ column density) with an inverted triangle.

radial bins discussed in the previous paragraph (Figure 16). The other exception is the region inward of 76 au toward HD 163296, where the fits with $T_{ex} = 30$ K underpredict the HCO^+ emission and overpredict the $H^{13}CO^+$ emission (Figure 16). Here, the models with T_{ex} as a free parameter provide a better fit and predict a column density smaller by a factor of a few compared to the fits where $T_{ex} = 30$ K.

In Figure 7, we also plot the column densities of CO that are derived from $C^{18}O$ $J = 2 - 1$ emission in Zhang et al. (2021). For each disk, they constructed a thermochemical model that reproduces the spectral energy distribution. The model provides the 2D (R, Z) distributions of temperature and CO abundance. Then, they introduced a CO depletion factor, which is varied from 0.001 to 50 with a step size of 1.1 in a logarithmic scale, at each radial bin, and calculated the CO flux for a grid of models to find the best-fit depletion factor. The uncertainty in the CO column density is thus 10% in most of the disk radii. Exceptions are the innermost and outermost radii; at these radii, the $C^{18}O$ line fluxes have relatively large uncertainties, and the error of the CO column density is 1σ. They also derived the CO column densities using the $J = 2 - 1$ transition of ^{13}CO and $J = 1 - 0$ transition of ^{13}CO, $C^{18}O$, and $C^{17}O$, which are in reasonable agreement with the value based on $C^{18}O$ ($J = 2 - 1$).

Overall, the radial profile of the HCO^+ column density is similar to that of CO. The panels in the middle row of Figure 7 show the column density ratio $N(HCO^+)/N(CO)$. Since the CO column density was calculated on a finer radial grid than HCO^+, we interpolated the CO column density at the radii of HCO^+. The error bars in the middle panels reflect only the error of HCO^+ column density, which dominates over that of CO column density. The ratio is mostly within 10^{-5}–10^{-4} at ~100–500 au, which suggests a close chemical link between these species, as expected from chemical models (e.g., Aikawa et al. 2015; Teague et al. 2015).

In the disk of IM Lup, the column densities of both HCO^+ and CO increase inward from $R \sim 500$ to 100 au, where the HCO^+/CO column density ratio is remarkably constant. The HCO^+ column density then declines at $\lesssim$100 au, while the CO column density becomes flat and rises inward at $\lesssim$50 au.

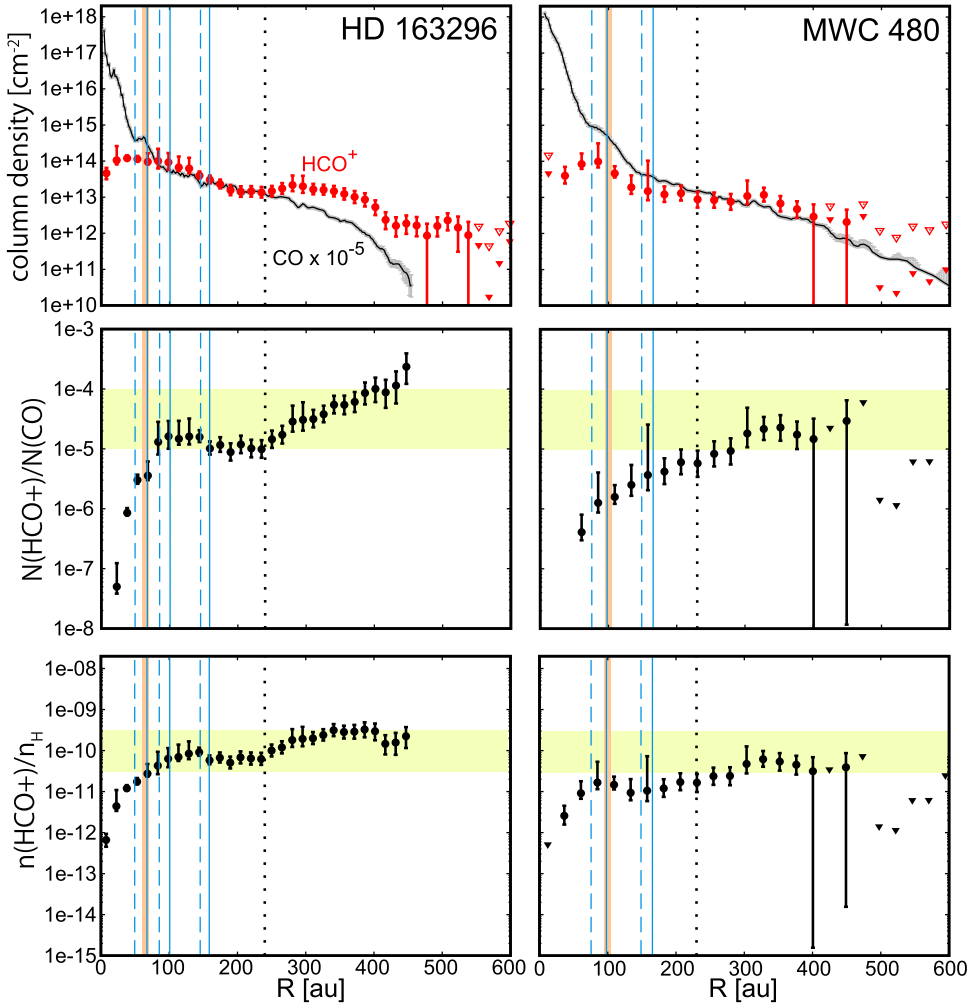

Figure 7. (Continued.)

In the GM Aur disk, the HCO^+/CO column density ratio exceeds 10^{-4} outside the dust continuum edge. Both the HCO^+ and CO column densities increase inward up to ∼100 au, while they have small local humps. At $R \sim 60$ au, the CO column density has a local maximum, while that of HCO^+ has a local minimum. This coincidence needs to be taken with caution, however, since the beam size of HCO^+ data is two times larger than that of CO, and since the column density estimates at the innermost radii suffer line broadening due to the velocity gradient within a beam. In the disk of AS 209, the radial profile of HCO^+ significantly differs from that of CO at $R \lesssim 100$ au. While the CO column density shows a broad depression at $R \sim 45$–120 au, the HCO^+ column density increases inward up to ∼75 au and stays constant at inner radii within the error bars. In the disk around HD 163296, the column density ratio of HCO^+/CO decreases inward up to $R \sim 240$ au, which corresponds to the edge of the millimeter dust continuum. From 240 to 65 au, the ratio stays constant or has a shallow rise, while both the CO and HCO^+ column densities increase inward. Inside the radius of ∼65 au, which coincides with the CO snow line in the thermochemical model, the HCO^+ column density is roughly constant, while the CO column density increases toward the center by more than an order of magnitude. The sharp rise of CO column density and relatively flat distribution of HCO^+ column density inside the CO snow line are also seen in MWC 480, while the overall column density ratio of HCO^+/CO is slightly lower than that in HD 163296. We note that the X-ray spectrum of MWC 480 is significantly softer than that of HD 163296 (Dionatos et al. 2019). Since X-rays are the major ionization source in the molecular layer (see Section 4.3), the relatively low HCO^+/CO column density ratio in MWC 480 could be due to the lack of high-energy X-rays (≳a few keV).

4. Discussion

4.1. HCO^+ Abundance in the Warm Molecular Layers

In the molecular layers of protoplanetary disks, the major molecular ions are H_3^+, HCO^+, and N_2H^+, among which H_3^+ cannot be observed at millimeter wavelengths. Its deuterated counterpart o-H_2D^+ has not been detected so far (e.g., Chapillon et al. 2011). Figure 8 shows the radial profiles of the HCO^+, N_2H^+, and N_2D^+ column densities obtained in this work and by Cataldi et al. (2021). We can see that HCO^+ has the largest column densities among the observable molecular ions in our five disks.

HCO^+ is expected to be the major molecular ion in the warm molecular layer where CO gas is abundant. Thus, here we assume that the majority of HCO^+ coexists with CO in the warm molecular layer and derive the HCO^+ abundance there, based on the HCO^+-to-CO column density ratio. Furthermore, we assume that the CO abundance relative to

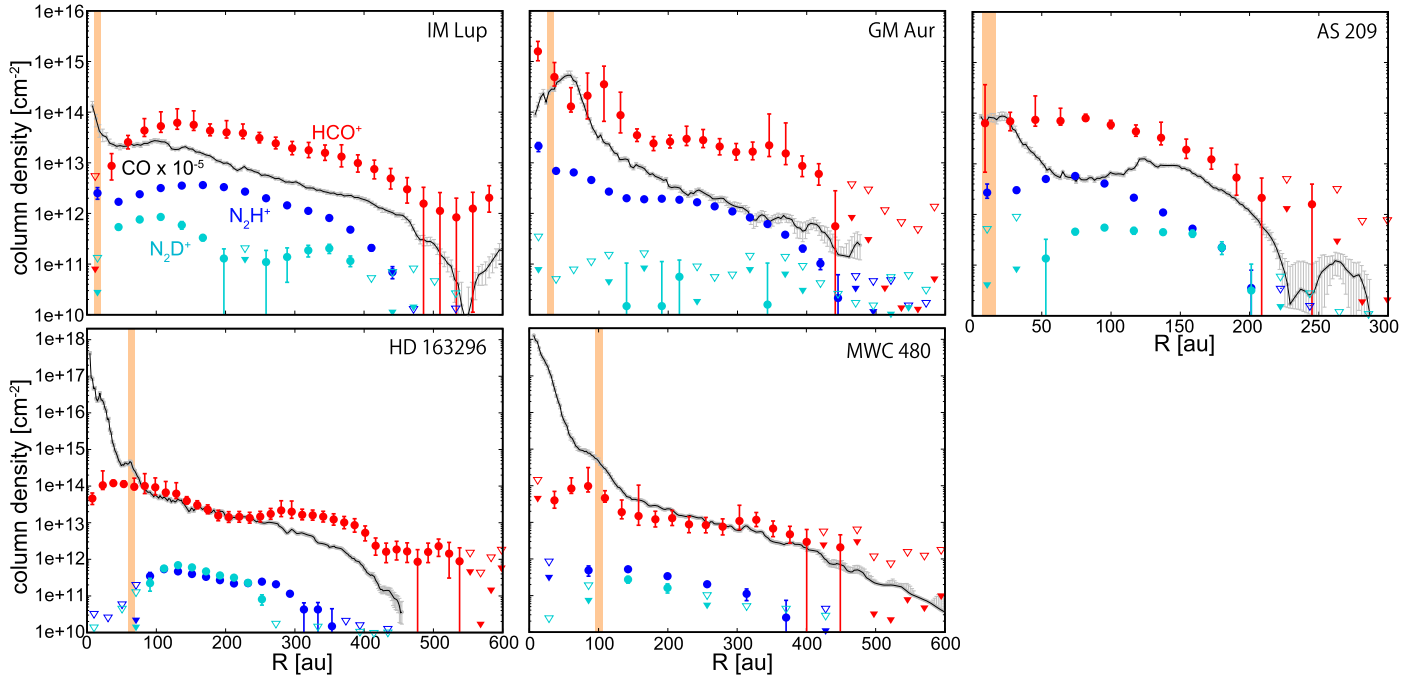

Figure 8. Column densities of HCO^+ (red), N_2H^+ (blue), and N_2D^+ (light blue). Black lines with gray error bars depict the CO column density scaled by 10^{-5}. The error bars correspond to 10% or 1σ for CO (see Section 3.2), while they show the 16th and 84th percentiles for other species. At radii where the median value of the molecular column density is lower than the value of the 16th percentile by a factor of >10, we plot the upper limits as inverted triangles (84th percentile for closed triangles and 98th percentile for open triangles). The vertical orange bars mark the CO snow line as inferred from the model by Zhang et al. (2021).

hydrogen nuclei is equal to its canonical abundance in molecular clouds, 5.0×10^{-5}, multiplied by the CO depletion factor derived in Zhang et al. (2021). The bottom panels in Figure 7 show the estimated HCO^+ abundance. Since the uncertainty (error) of the HCO^+ column density dominates over that of the CO column density at most disk radii, and since the methods of error estimation are different between HCO^+ and CO, we evaluate the error of the HCO^+ abundance considering only that of the HCO^+ column density. Overall, the HCO^+ abundance is in a range of $3 \times 10^{-11} - 3 \times 10^{-10}$ outside ~100 au and tends to decline toward the disk center at the inner radii.

In those inner regions, the CO-rich molecular layer extends toward the midplane, although detailed analysis by Zhang et al. (2021) shows that the gaseous CO fractional abundance does not necessarily recover its canonical value (i.e., 10^{-4} relative to H_2) even inside of the CO snow line. Closer to the midplane, the gas density is higher and the ionization degree, i.e., the HCO^+ abundance, should be lower. Furthermore, HCO^+ is suppressed by grain-surface recombination (i.e., collision with a negatively charged grain), which could be more efficient than the recombination in the gas phase at high densities. The HCO^+ abundance averaged over the CO gas-rich layer should thus be lower around and inside the CO snow line than at outer radii (see Section 4.3).

Although HCO^+ is expected to be one of the major molecular ions in the warm molecular layer, it is not always the most abundant ion. The relative abundances of major molecular ions, H_3^+, HCO^+, and N_2H^+, are determined by the balance between proton transfer and recombination of relevant species, i.e., H_2, CO, and N_2 (Aikawa et al. 2015). Furthermore, if the abundance of small grains is low enough to allow significant penetration of UV radiation, atomic ions such as C^+ and S^+ can dominate even in the CO-rich layers (e.g., Aikawa et al. 2015). Therefore, the HCO^+ abundance derived here should be considered as a lower limit of the ionization degree in the molecular layer.

4.2. HCO^+ Enhancement in Gas Gaps

The HCO^+ abundance exceeds 10^{-9} at 50 au $\lesssim R \lesssim$ 150 au in AS 209, where the CO column density shows a depression. Favre et al. (2019) observed DCO^+ $J = 3 - 2$ in AS 209 with high resolution ($0\farcs26 \times 0\farcs21$) and found a ring-like emission with its peak at ~85 au. They suggest that the overdensity of DCO^+ is caused by the more efficient ionization at the radius of gas and dust depletion, which is carved by a planet of $\lesssim$0.3 $M_{\rm Jup}$ at ~100 au. The high HCO^+ abundance at 50 au $\lesssim R \lesssim$ 150 au is consistent with their scenario.

Alarcón et al. (2021), on the other hand, calculated the thermal structure in two disk models for AS 209; model A assumes a smooth gas distribution and a CO abundance drop around $R \sim 80$ au, while model B assumes a constant CO abundance combined with a gas density drop around 80 au. They found that the radial pressure profile derived by Teague et al. (2018b) is shallower than in model B and concluded that the CO column density drop at 80 au is caused mainly by a CO abundance drop rather than a gas density drop. Self-consistent modeling of the thermal structure and the HCO^+ and DCO^+ chemistry would be useful to distinguish between these scenarios.

We also note correlated local enhancements of HCO^+ and DCO^+ in HD 163296. Flaherty et al. (2017) observed DCO^+ ($J = 3 - 2$) with a beam of $0\farcs5 \times 0\farcs59$ and found that DCO^+ emission is confined to three concentric rings at 54, 124, and 214 au. The ring at 124 au is the brightest and coincides with the shoulder seen in HCO^+ emission in Figure 3 and the local enhancement of the HCO^+/CO column density ratio (Figure 7). Teague et al. (2018a) analyzed the disk gas kinematics around HD 163296 and found deviations from Keplerian rotation, which

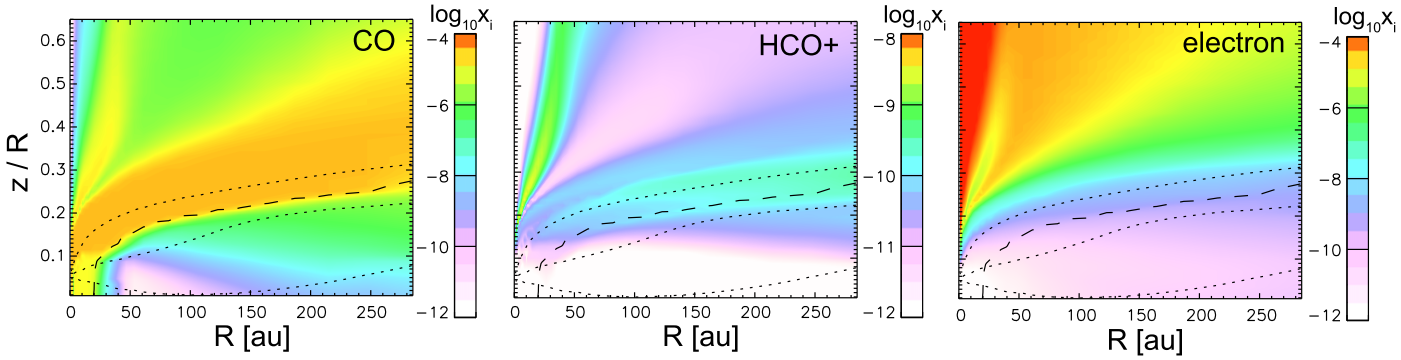

Figure 9. The abundances of CO (left), HCO^+ (middle), and electrons (right) relative to hydrogen nuclei in the low-ζ model. The dashed line depicts the CO snow surface, and the dotted lines show the positions where the X-ray ionization rate is 5×10^{-17} (the upper dotted line), 1×10^{-18} (the middle dotted line), and 1×10^{-19} s^{-1} (the lower dotted line),

suggests the presence of a 1 $M_{\rm Jup}$ planet at 83 au and a 1.3 $M_{\rm Jup}$ planet at 137 au. Hydrodynamic models of the HD 163296 disk with these planets show gas gaps (i.e., gas density decrease) around the planet orbits. The local enhancement of DCO^+ and HCO^+ around 125 au could be related to such gas gaps.

In MWC 480, the CO column density shows a local minimum around the gap seen in dust continuum at ~76 au (Figure 7). We note that the HCO^+ column density has a local maximum at this radius; we derived the column density distribution with radial grids of a quarter of the beam size to confirm the coincidence. It again suggests a correlation between gas gap and HCO^+ enhancement. Observations of HCO^+ with higher angular resolution are desirable for further studies.

4.3. Constraining the Ionization Structure with a Template Disk Chemistry Model

MAPS observations, as well as previous ALMA observations of disks in the past few years, show that detailed physical structure, e.g., size, flaring, and temperature structure, varies significantly among disks (e.g., Law et al. 2021b). While source-specific modeling is desirable, it is out of the scope of the present work. However, we note that the derived abundance and its radial distribution of HCO^+ have common features; the HCO^+ abundance is $\sim 3 \times 10^{-11} - 3 \times 10^{-10}$ at $\gtrsim$100 au, while it tends to decrease inward at smaller radii. These features should reflect the basic chemistry of HCO^+, which is not very sensitive to the details of the disk structure. Therefore, we compare our results with some template disk models.

We adopt the disk chemistry model of Aikawa et al. (2018); the disk mass is 1.7×10^{-2} $M_\odot$, and the mass of the central star is 0.5 $M_\odot$. Stellar UV and X-ray luminosities are 10^{31} and 10^{30} erg s^{-1}, respectively. While the dust sedimentation is not considered, the maximum grain size is set to be 1 mm. Since the total gas-to-dust mass ratio is set to be the same as the interstellar value (~100), the abundance of small dust grains is reduced compared with the interstellar dust. The 2D (R,Z) distributions of the gas number density (i.e., number density of hydrogen nuclei $n_{\rm H}$) and temperature are shown in Figure 19 in Appendix E. While Aikawa et al. (2018) varied several parameters in the calculation of the chemistry model, we here show three models: their fiducial model, a high-C/O model, and a low-ζ model, which is newly calculated for the present work. The fiducial model is a static disk model with a CR ionization rate of 5×10^{-17} s^{-1}. Two other ionization sources, X-rays and the decay of SLRs, are included in the model with the X-ray spectrum of TW Hya and the ionization rate by SLRs of $\zeta_{\rm SLR} = 1 \times 10^{-18}$ s^{-1}. The initial molecular abundance for the disk chemistry is set by calculating the chemical evolution from the molecular cloud formation stage to the collapse of a star-forming core. In the fiducial model, the elemental abundances of C and O are 7.82×10^{-5} and 1.8×10^{-4}, respectively, relative to hydrogen nuclei (i.e., C/O = 0.43). Disk observations in recent years, however, suggest low C/H ratios and high C/O ratios in the gas phase (e.g., Bergin et al. 2014, 2016; Bosman et al. 2021; Zhang et al. 2021). This is likely due to the removal of ice by the sedimentation and radial migration of ice-coated pebbles (Kama et al. 2016; Krijt et al. 2018). Thus, in the high-C/O model, H_2O is completely removed and CO is reduced by one order of magnitude in the initial molecular abundances, which results in a C/O ratio of 1.43. In addition to these two models, we run a low-ζ model, in which the CR ionization rate is set to zero. Ionization rates by X-ray and SLRs are set to be the same as in the fiducial model, and the initial molecular abundance is the same as the high-C/O model. Since we aim to constrain the ionization rate rather than identifying the main ionization source, the low-ζ model can simply be considered as a model with a midplane ionization rate of $\zeta_{\rm mid} = 10^{-18}$ s^{-1}, while $\zeta_{\rm mid}$ is 5×10^{-17} s^{-1} in the fiducial model and high-C/O model.

While molecular evolution in the disk is calculated up to $t = 1 \times 10^6$ yr, we compare our observational results with the molecular abundances at $t = 1 \times 10^5$ yr, which is comparable to the vertical mixing timescale at the radius of several tens of au assuming an α parameter of 10^{-3} for turbulent mixing (e.g., Aikawa et al. 1996). In gas-grain chemical networks, volatile species tend to be converted to less volatile ices. At $t = 10^6$ yr, a significant amount of CO and N_2 is converted to CO_2, CH_3OH, and NH_3, which could be an artifact of the static disk assumption (i.e., without mixing or accretion). The desorption rate and thermal diffusion rate (and thus the reaction rate) on the grain surface are very sensitive to temperature. In the static model, in which gas and dust stay at the same position and thus are kept at a constant temperature, only a limited number of species can effectively diffuse and react, which results in an accumulation of specific products. At $t = 1 \times 10^5$ yr, such accumulations are less significant (see Aikawa et al. 2015, for more details).

Figure 9 shows the abundances of CO, HCO^+, and electrons relative to hydrogen nuclei, in the low-ζ model. The abundances in the other models are shown in Figure 19 in Appendix E. We can see that CO and HCO^+ are mostly cospatial and that the observed features are reproduced; the HCO^+/CO abundance ratio is $\sim 10^{-5}$–10^{-4}, and the HCO^+ abundance is $\sim 10^{-10}$ in the lower part of the CO-rich layer, where the density is higher. In Figure 9, the dashed line

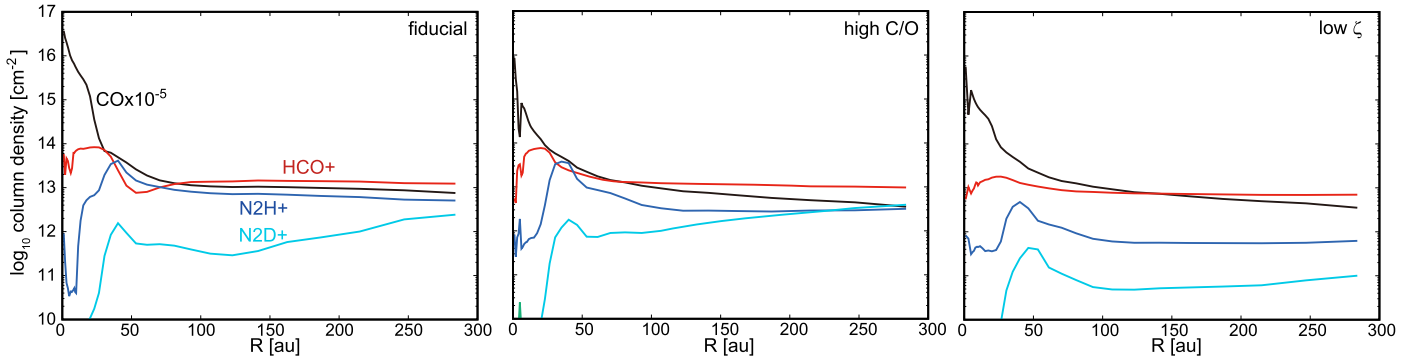

Figure 10. Column densities of CO (multiplied by 10^{-5}), HCO^+, N_2H^+, and N_2D^+ in the fiducial model (left), high-C/O model (middle), and low-ζ model (right).

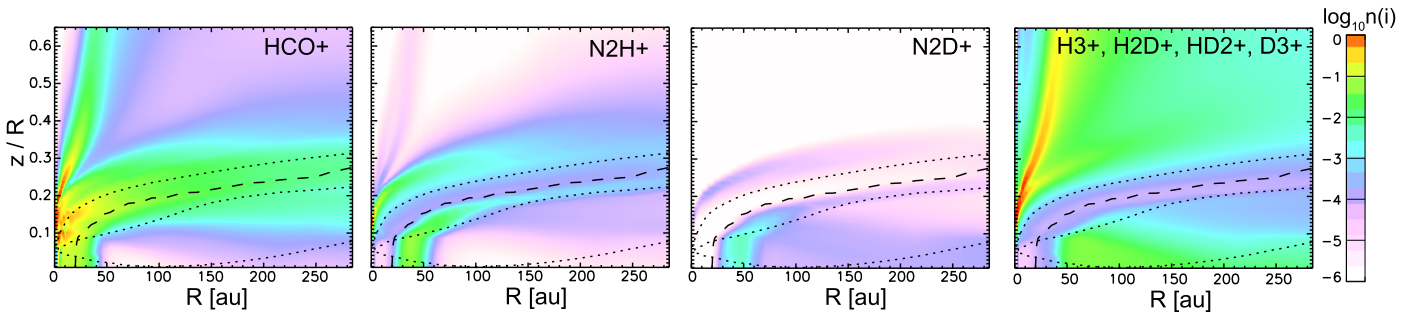

Figure 11. The absolute abundances (number densities) of HCO^+, N_2H^+, N_2D^+, and H_3^+ (and its deuterated isotopomers) relative to hydrogen nuclei in the low-ζ model. The dashed line depicts the CO snow surface, and the dotted lines depict the position where the X-ray ionization rate is 5×10^{-17} (the upper dotted line), 1×10^{-18} (the middle dotted line), and 1×10^{-19} s^{-1} (the lower dotted line).

depicts the CO snow surface, and the dotted lines depict the position where the X-ray ionization rate is 5×10^{-17} (upper), 1×10^{-18} (middle), and 1×10^{-19} s^{-1} (lower). We note that the dashed line and dotted lines are roughly parallel at radii >50 au, probably because both parameters are controlled by the radiation transfer from the central star (i.e., stellar irradiation and X-rays). Inside the CO snow line (where the dashed line crosses the midplane), CO is indeed abundant near the midplane, although its abundance is reduced by an order of magnitude compared to the initial value ($\sim 10^{-5}$) owing to the conversion to less volatile species such as CO_2 ice. In this region, the HCO^+/CO abundance ratio is less than 10^{-5} in the low-ζ model, which is also consistent with the observations. Comparing the HCO^+ and the electron abundances, we can see that the former is slightly lower than the latter even in the layers where the HCO^+ abundance peaks. This means that the ionization degree is actually higher than the HCO^+ abundance; atomic ions are relatively abundant even in the CO-rich layer in the model.

Figure 10 shows the radial profiles of the column densities of CO (multiplied by 10^{-5}), HCO^+, N_2H^+, and N_2D^+ in the three models. As references, 2D distributions of absolute abundances (i.e., number densities) of major molecular ions in the low-ζ model are shown in Figure 11. Similar plots for the other two disk models are shown in Figure 20 in Appendix E. The column densities in the models are almost constant outside ~100 au, while the observed values decline outward. This discrepancy might arise because the model gas density is not exponentially tapered, but simply follows a power law up to a radius of 284 au. We thus only compare the model column densities inside ~200 au with the observed values. In all three models, the radial profile of the column density ratio $N(HCO^+)/N(CO)$ is similar to those in Figure 7; $N(HCO^+)/N(CO)$ is nearly constant ($\sim 10^{-5}$) but declines toward the disk center inside a certain radius, which corresponds to the CO snow line in the disk models.

Figure 10 shows that at radii outside the CO snow line (~20 au in the template model) the HCO^+ column density is not sensitive to ζ_{mid}, since the contribution of the X-ray ionized region is significant in the CO-rich layer there (see Figures 11 and 20). Inside the CO snow line, the CO-rich layer extends to the midplane. The HCO^+ column density and the gas column density ratio $N(HCO^+)/N(CO)$ around and inside the CO snow line are thus more sensitive to ζ_{mid}.[27] The peak value of the HCO^+ column density is lower in the low-ζ model than in the models with $\zeta_{mid} = 5 \times 10^{-17}$ s^{-1} by a factor of 4.6 (fiducial model) and 4.2 (high-C/O model). The column density ratio of HCO^+/CO at the HCO^+ column density peak is also lower in the low-ζ model accordingly. Around the CO snow lines predicted from the thermochemical model of Zhang et al. (2021), the HCO^+ column density derived from the observation is $\gtrsim 10^{14}$ cm^{-2} with the column density ratio of $HCO^+/CO \sim 10^{-5}$ in our targeted disks, as in our fiducial model or high-C/O model, except for those around IM Lup and MWC 480. It may suggest $\zeta_{mid} \sim 10^{-17}$ s^{-1} around the CO snow line. We note, however, that the HCO^+ column density would also depend on the total gas column density, which is not varied in the set of template models shown here. While the mass of the template disk model is within the range of estimated values for GM Aur and IM Lup, AS 209 is less massive and the disks around the Herbig Ae stars are more massive (Zhang et al. 2021) (see Section 4.4). Source-specific models are needed for further comparison.

[27] We note that the absolute abundance of HCO^+ in the midplane is high even at radii slightly outside the CO snow line. For HCO^+ to be the abundant ion, CO does not need to fully sublimate to the gas phase (Aikawa et al. 2015).

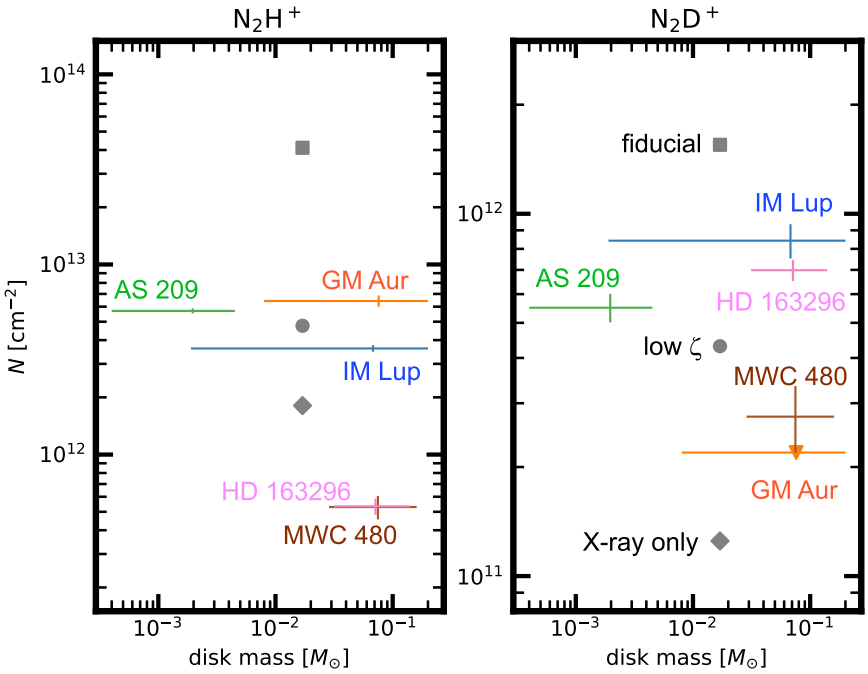

Figure 12. The N_2H^+ and N_2D^+ column densities as a function of disk mass. For each disk, a mass range adopted from Zhang et al. (2021) is shown as the horizontal error bar. The column densities correspond to the peak values, with the error bars indicating the 16th and 84th percentiles. For N_2D^+ in GM Aur, we instead plot the 99.85th percentile at ∼100 au as an upper limit. Predictions from the template models are shown by the gray points.

4.4. Ionization Rate Traced by N_2H^+ and N_2D^+

The template disk models (Figures 10, 11, and 20) indicate that, in contrast to HCO^+, the column densities of N_2H^+ and N_2D^+ are more sensitive to the ionization rate below the CO snow surface, where these molecular ions are relatively abundant. In the cold midplane, H_3^+ and its deuterated isotopomers are the most abundant ions, but H_3^+ and D_3^+ are not observable at radio wavelengths, and H_2D^+ and HD_2^+ are not detected so far, possibly due to unfavorable o/p ratios (e.g., Chapillon et al. 2011). Figure 20 shows that among the observable molecular ions, N_2D^+ is the best proxy of deuterated H_3^+ and thus the best probe of ionization rate in the midplane. Although its abundance is lower than the sum of H_3^+ and its deuterated isotopomers, the gas above the CO snow surface does not significantly contribute to its column density in our template disk models. In the template disk models, the N_2H^+ and N_2D^+ column densities have a peak around $R \sim 50$ au, where these molecular ions are abundant in the midplane (see also Qi et al. 2019). This indicates that $\zeta_{\rm mid}$ could be best investigated by their peak column densities, especially by the N_2D^+ column density.

The column densities of N_2H^+ and N_2D^+ in our target disks are derived by Cataldi et al. (2021) and are plotted in Figure 8. As expected from the template disk models, these column densities have a peak outside the CO snow line, except for GM Aur, for which the N_2H^+ column density is the highest at the innermost radial grid. The value at the innermost grid could, however, be overestimated, since these column densities are derived by assuming a fixed excitation temperature of 20 K. When the excitation temperature is set to be the same as the midplane temperature of the thermochemical model of Zhang et al. (2021), the N_2H^+ column density has a peak ($\sim 10^{13}$ cm^{-2}) around $R \sim$ 100 au (Cataldi et al. 2021).

Unlike HCO^+, the distributions of N_2H^+ and N_2D^+ are expected to anticorrelate with that of CO. We thus consider their column densities rather than the column density ratio to CO. In Figure 12, we plot the peak N_2H^+ and N_2D^+ column densities derived by Cataldi et al. (2021) versus disk mass to see whether there is any trend. For each disk, a range of possible masses is shown, extending from the minimum masses to the best-fit mass given in Tables 3 and 2 of Zhang et al. (2021), respectively. While the estimated disk masses of IM Lup, GM Aur, HD 163296, and MWC 480 overlap with each other,[28] their N_2H^+ and N_2D^+ peak column densities vary, which indicates that the midplane ionization rate varies among the disks. The gray squares and circles depict the peak column densities around $R \sim 50$ au in the fiducial model and low-ζ model, respectively. The gray diamonds show the values in the model with X-ray ionization only, i.e., the midplane ionization rate is $\lesssim 10^{-19}$ s^{-1}. The peak column densities of the high-C/O model are not plotted but are similar to those of the fiducial model.

The N_2H^+ column densities of IM Lup, GM Aur, and AS 209 indicate $\zeta_{\rm mid} \sim 10^{-18}$ s^{-1}. For MWC 480 and HD 163296, the N_2H^+ column density is lower than that of the X-ray-only model, which indicates that the X-ray ionization is less effective in these disks than in our template models. We note that a fraction of N_2H^+ exists in the layer with relatively high X-ray ionization rate ($\gtrsim 5 \times 10^{-17}$ s^{-1}), which sets the floor value of the N_2H^+ column density in our template models. For MWC 480, the low N_2H^+ column density is consistent with its soft X-ray spectrum and relatively low HCO^+ column density. An alternative explanation for the variety of N_2H^+ column density would be the temperature structure in the disk. The column density of N_2H^+ should be lower if the midplane layer of the low temperature ($\lesssim$20 K) is thinner (Qi et al. 2019). This could be the case for the MWC 480 disk, in which both N_2H^+ and N_2D^+ column densities are

[28] Fedele et al. (2018) reproduced their 1.3 mm dust continuum image with a disk model with a dust mass of $3.5 \times 10^{-4}\ M_\odot$. If the gas-to-dust mass ratio is 100, the disk mass of AS 209 is also similar to the disk mass of IM Lup and GM Aur.

low. HD 163296, on the other hand, has relatively high column density of N_2D^+, which indicates that there is plenty of cold gas in the midplane (see below).

The N_2D^+ peak column densities of IM Lup, AS 209, and HD 163296 are similar to or slightly larger than the value from the low-ζ model, which suggests $\zeta_{\rm mid} \gtrsim 10^{-18}$ s^{-1}. In the HD 163296 disk, the peak N_2D^+ column density is relatively high, while the low N_2H^+ column density indicates lower X-ray ionization rate than the template models. The midplane ionization rate, which is better traced by N_2D^+, would thus be set by SLRs or high-energy particles. In GM Aur, on the other hand, the upper limit of N_2D^+ column density indicates a low ionization rate ($<10^{-18}$ s^{-1}) in the midplane.

Finally, we note that the N_2H^+ and N_2D^+ column densities depend not only on $\zeta_{\rm mid}$ but also on other parameters such as the vertical temperature distribution and the disk mass (Cleeves et al. 2014; Qi et al. 2019). Source-specific models are needed to estimate the midplane ionization rate more quantitatively for each object.

5. Conclusions

We observed and analyzed HCO^+ $J = 1 - 0$ and $H^{13}CO^+$ $J = 1 - 0$ lines toward the protoplanetary disks around IM Lup, GM Aur, AS 209, HD 163296, and MWC 480. $H^{13}CO^+$ $J = 1 - 0$ was detected in all five disks, while $H^{13}CO^+$ $J = 1 - 0$ was detected ($S/N > 6\sigma$) toward GM Aur and HD 163296 and tentatively detected ($S/N > 3\sigma$) toward the other disks by a matched filter analysis in the u-v plane. The disk-integrated flux of $H^{13}CO^+$ $J = 1 - 0$ is also above 3σ in IM Lup, GM Aur, and HD 163296.

We derived the HCO^+ column density by fitting the azimuthally averaged spectra of HCO^+ and $H^{13}CO^+$ simultaneously for radial bins of half the beam FWHM. In all five disks, the HCO^+ column density increases inward but becomes flat or drops toward the center inside a radius of $R \sim 100$ au. The column density ratio of $N(HCO^+)/N(CO)$ is about 10^{-5}–10^{-4} at $R \gtrsim 100$ au, except for the MWC 480 disk, in which the column density ratio is $<10^{-5}$ at $R \lesssim 200$ au.

We derived the HCO^+ abundance in the warm CO-rich layer, where HCO^+ is expected to be the dominant molecular ion, via the column density ratio $N(HCO^+)/N(CO)$ using the radial profiles of CO column density and CO depletion factor from Zhang et al. (2021). Beyond ~100 au, the derived HCO^+ abundance ranges from 3×10^{-11} to 3×10^{-10} in the IM Lup, GM Aur, and HD 163296 disks. The HCO^+ abundance is lower in MWC 480, possibly due to the lack of high-energy (> a few keV) X-rays. The HCO^+ abundance tends to decline toward the disk center for $R \lesssim 100$ au. This can be explained by the lower ionization degree in denser gas, especially inside the CO snow line, where the CO-rich layer is in the midplane.

We find a hint of a correlation between the HCO^+ abundance and the gap carved by a putative planet in AS 209: the HCO^+ abundance exceeds 10^{-9} at $R \sim 50$–150 au, where the CO column density is depressed. This region seems to correspond to the gas gap, where ionization would be more efficient. In HD 163296, the HCO^+ abundance shows a shallow bump at 100–150 au, which coincides with the radius of DCO^+ enhancement found by Flaherty et al. (2017). This feature could also be related to the enhanced ionization around a gas gap. In MWC 480, the HCO^+ column density has a local maximum at ~76 au, which coincides with the local depression of CO and the gap seen in the dust continuum.

Finally, we compared the column densities of HCO^+, N_2H^+, and N_2D^+ with those of template disk models: a fiducial disk model with a midplane ionization rate $\zeta_{\rm mid}$ of 5×10^{-17} s^{-1}, a model with CO and H_2O depletion, and a model with $\zeta_{\rm mid} = 1 \times 10^{-18}$ s^{-1}. The almost constant HCO^+ abundance at $R \gtrsim 100$ au is explained by X-ray ionization in the CO-rich layer. The decline of the HCO^+ abundance at the inner radii, on the other hand, can be explained by CO sublimation inside the CO snow line; the CO-rich layer then extends to the midplane, where the ionization degree is low owing to high density. While the estimated disk mass ranges of IM Lup, GM Aur, HD 163296, and MWC 480 overlap with each other, their peak column densities of N_2H^+ and N_2D^+ vary, which may indicate that the midplane ionization rate varies among disks. The peak N_2D^+ column density suggests a midplane ionization rate of $\gtrsim 10^{-18}$ s^{-1} for IM Lup, AS 209, and HD 163296, while the upper limit of N_2D^+ column density indicates that it is $<10^{-18}$ s^{-1} for GM Aur. The peak column density of N_2H^+ is lower in MWC 480 than in other disks, which is consistent with its soft X-ray spectrum and relatively low HCO^+ column density. Alternatively, the low column densities of N_2H^+ and N_2D^+ in the MWC 480 disk could be due to its warmer temperature, i.e., the cold midplane layer is thinner than in other disks. Source-specific models are needed for further evaluation of the midplane ionization rate.

This paper makes use of the following ALMA data: ADS/JAO.ALMA#2018.1.01055.L, ADS/JAO.ALMA2015.1.00678.S, ADS/JAO.ALMA#2012.1.00681.S, ADS/JAO.ALMA#2015.1.00657.S. ALMA is a partnership of ESO (representing its member states), NSF (USA) and NINS (Japan), together with NRC (Canada), MOST and ASIAA (Taiwan), and KASI (Republic of Korea), in cooperation with the Republic of Chile. The Joint ALMA Observatory is operated by ESO, AUI/NRAO and NAOJ. This research has made use of NASA's Astrophysics Data System and the SIMBAD database, operated at CDS, Strasbourg, France.

We would like to thank the anonymous referee for careful reading of our manuscript and for constructive comments. Y.A. acknowledges support by NAOJ ALMA Scientific Research grant code 2019-13B, Grant-in-Aid for Scientific Research (S) 18H05222, and Grant-in-Aid for Transformative Research Areas (A) 20H05844 and 20H05847. G.C. is supported by the NAOJ ALMA Scientific Research grant code 2019-13B. Y.Y. is supported by IGPEES, WINGS Program, the University of Tokyo. K.Z. acknowledges the support of the Office of the Vice Chancellor for Research and Graduate Education at the University of Wisconsin−Madison with funding from the Wisconsin Alumni Research Foundation. K.Z., K.R.S., J.H., J.B., J.B.B., and I.C. acknowledge the support of NASA through Hubble Fellowship grants HST-HF2-51401.001, HST-HF2-51419.001, HST-HF2-51460.001-A, HST-HF2-51427.001-A, HST-HF2-51429.001-A, and HST-HF2-51405.001-A awarded by the Space Telescope Science Institute, which is operated by the Association of Universities for Research in Astronomy, Inc., for NASA, under contract NAS5-26555. A.S.B. acknowledges the studentship funded by the Science and Technology Facilities Council of the United Kingdom (STFC). S.M.A. and J.H. acknowledge funding support from the National Aeronautics and Space Administration under grant No. 17-XRP17 2-0012 issued through the Exoplanets Research Program. E.A.B. and A.D.B. acknowledge support from NSF AAG grant No. 1907653. L.I.C.

gratefully acknowledges support from the David and Lucille Packard Foundation and Johnson & Johnson's WiSTEM2D Program. V.V.G. acknowledges support from FONDECYT Iniciación 11180904 and ANID project Basal AFB-170002. J. D.I. acknowledges support from the Science and Technology Facilities Council of the United Kingdom (STFC) under ST/T000287/1. C.J.L. acknowledges funding from the National Science Foundation Graduate Research Fellowship under grant No. DGE1745303. R.L.G. acknowledges support from a CNES fellowship grant. F.M. acknowledges support from ANR of France under contract ANR-16-CE31-0013 (Planet-Forming-Disks) and ANR-15-IDEX-02 (through CDP "Origins of Life"). H.N. acknowledges support by NAOJ ALMA Scientific Research grant code 2018-10B and Grant-in-Aid for Scientific Research No. 18H05441. K.I.Ö. acknowledges support from the Simons Foundation (SCOL No. 321183) and an NSF AAG grant (No. 1907653).
R.T. acknowledges support from the Smithsonian Institution as a Submillimeter Array (SMA) Fellow. T.T. is supported by JSPS KAKENHI grant Nos. JP17K14244 and JP20K04017. C.W. acknowledges financial support from the University of Leeds, STFC and UKRI (grant Nos. ST/R000549/1, ST/T000287/1, and MR/T040726/1).
Facility: ALMA.

Software: Astropy (Astropy Collaboration et al. 2013; Price-Whelan et al. 2018), bettermoments (Teague & Foreman-Mackey 2018), CASA (McMullin et al. 2007), emcee (Foreman-Mackey et al. 2013), gofish (Teague 2019), matplotlib (Hunter 2007), NumPy (van der Walt et al. 2011), pythonradex (https://github.com/gica3618/pythonradex), SciPy (Virtanen et al. 2020), SPECTCOL (VAMDC Consortium, http://www.vamdc.org), VISIBLE (Loomis et al. 2018).

Appendix A
Hybrid Zeroth-moment Maps with a 0.″5 Beam

While we used the data cubes tapered to a circular 0.″3 beam for the analysis, faint emission is better recognized in images with lower spatial resolution. Since Band 3 lines tend to be fainter than Band 6 lines, the MAPS collaboration also produced the data cube tapered to a circular 0.″5 beam for Band 3 lines (Öberg et al. 2021; Czekala et al. 2021). Figure 13 shows the hybrid zeroth-moment maps of the $J = 1 - 0$ lines of HCO^+ and $H^{13}CO^+$ tapered to a circular 0.″5 beam. All maps were produced by combining a Keplerian mask and a smoothed 0σ-clip mask (Law et al. 2021a).

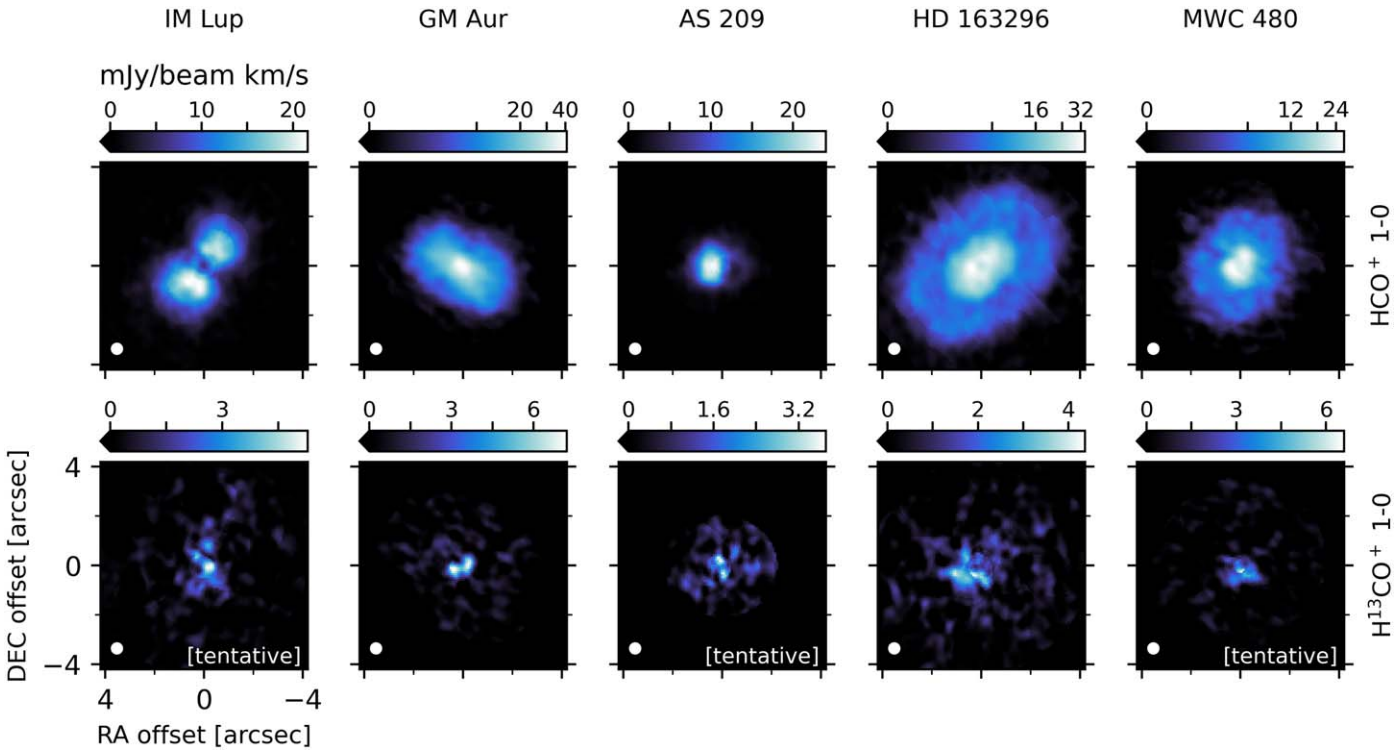

Figure 13. Same as Figure 2, but for images tapered to a circular 0.″5 beam.

Appendix B
Matched Filter Analysis and Disk-integrated Spectra for $H^{13}CO^+$ $J = 1 - 0$

The $J = 1 - 0$ line of $H^{13}CO^+$ is not clearly seen in our zeroth-moment maps (Figure 2), radial emission profiles (Figure 3), or azimuthally averaged spectra (Figure 16). To test whether the line is detected, we applied a matched filter analysis in the u-v plane (Loomis et al. 2018; see also Czekala et al. 2021). We calculate the visibilities of a Keplerian disk model, which are then cross-correlated with the observed visibilities to produce a response for each channel of the data. The response spectrum is then divided by the rms of the response spectrum at signal-free regions. Since we do not know the radial distribution of the emission, we computed the filter response for a series of Keplerian disk models with varying radial extents to find the Keplerian model that maximizes the S/N at the systemic velocity. Figure 14 shows the matched filter responses with the maximum S/N, while the radial extent of the corresponding Keplerian disk models is shown in the figure and also listed in Table 2. We note that the radial extent of the Keplerian disk model roughly represents the radial extent of the emission. $H^{13}CO^+$ $J = 1 - 0$ is detected with an S/N above 6σ for GM Aur and HD 163296. The line is tentatively detected with an S/N above 3σ for IM Lup, AS 209, and MWC 480.

In Figure 15 we show the shifted and azimuthally averaged, disk-integrated $H^{13}CO^+$ $J = 1 - 0$ spectrum of each disk. The radial extent of the region over which we averaged is the same as for the matched filter. The disk-integrated spectra also point oward a detection in GM Aur and HD 163296, although at lower significance than the matched filter. In summary, we detect $H^{13}CO^+$ $J = 1 - 0$ toward GM Aur and IM Lup and tentatively detect it toward the other three disks.

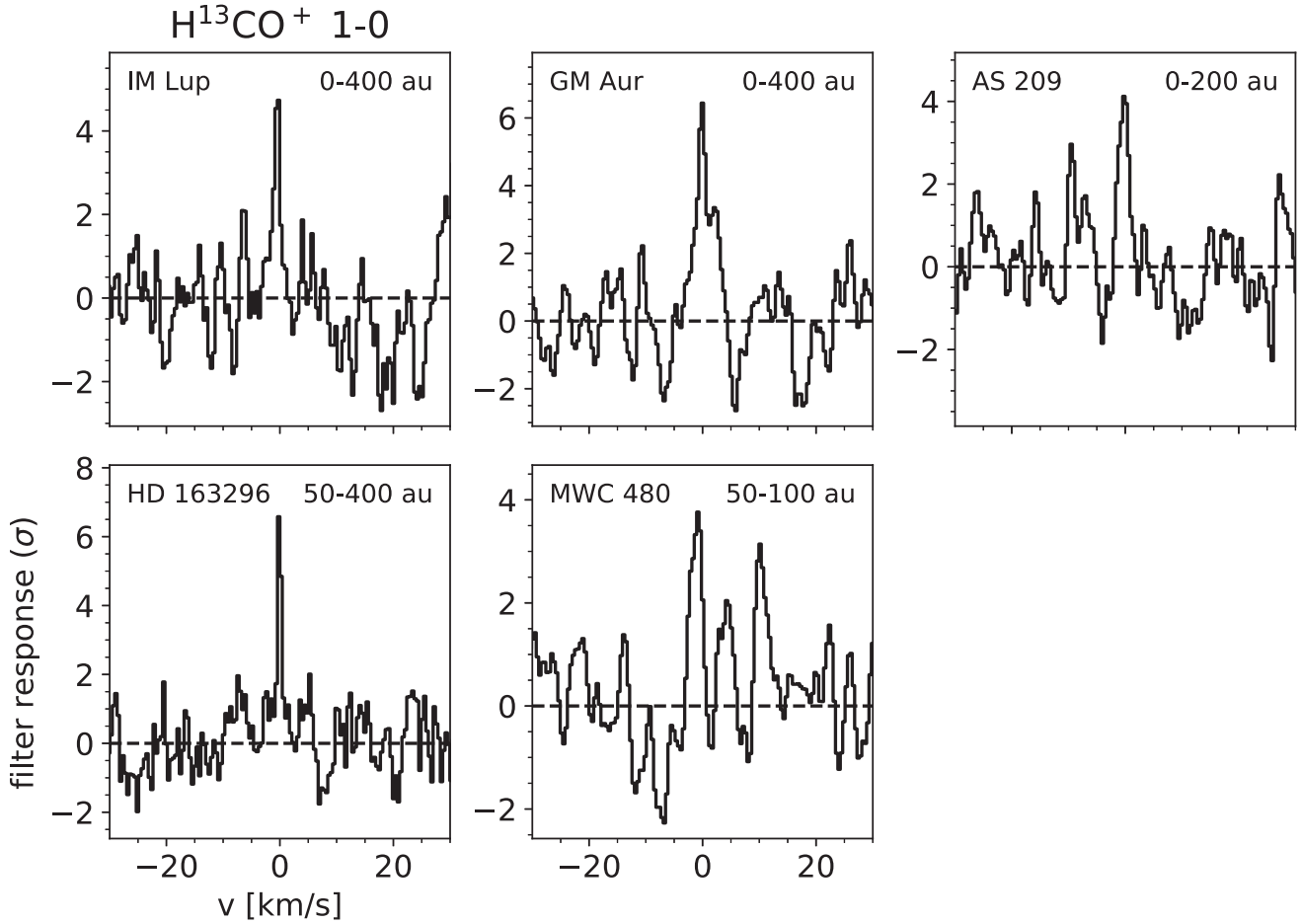

Figure 14. Matched filter response for $H^{13}CO^+$ $J = 1 - 0$. For each disk, we chose the Keplerian mask with the radius that maximized the S/N. The radial extent of that model is indicated in the upper right corner of each panel. The y-axis is in units of the noise in the filter response.

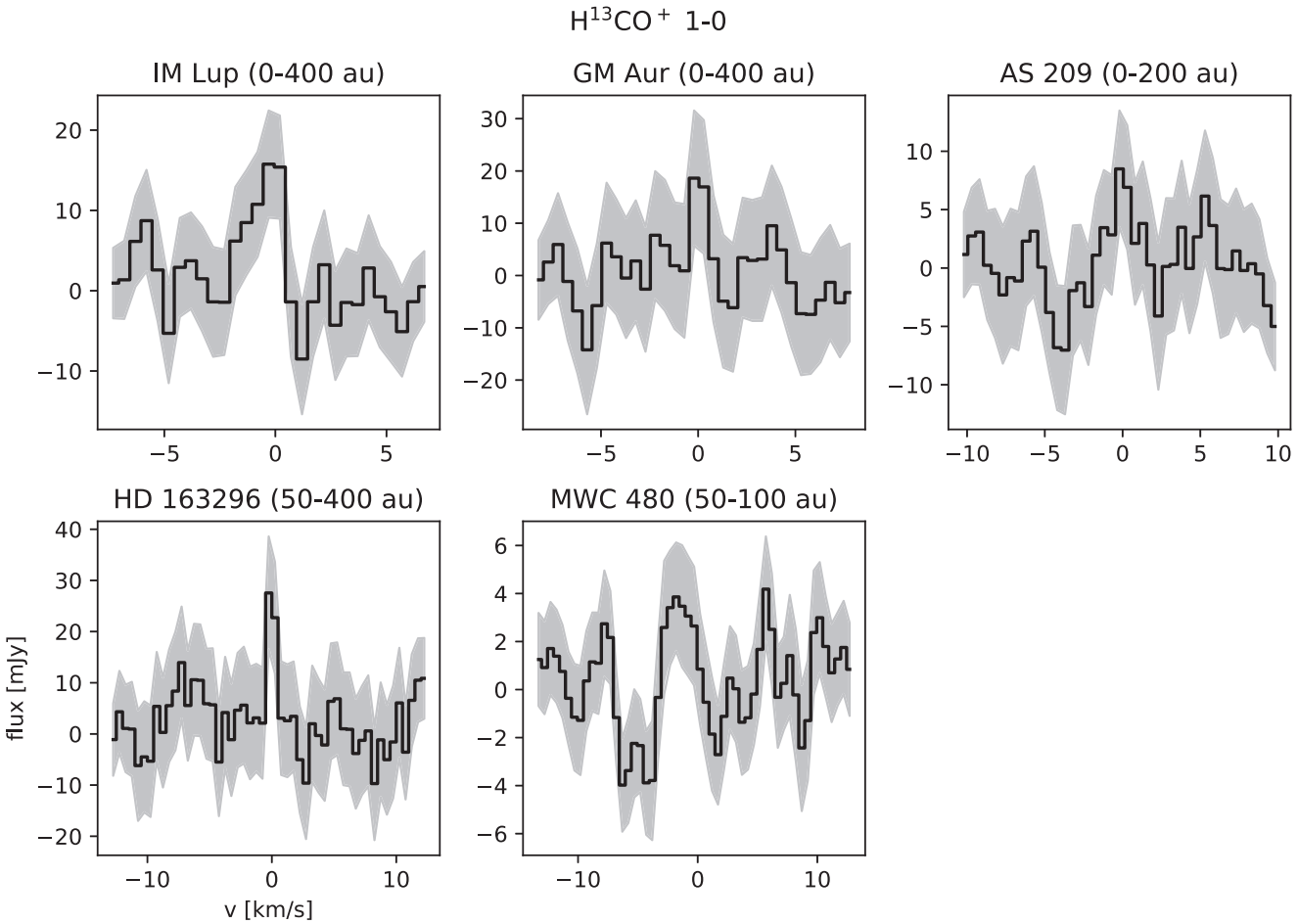

Figure 15. Disk-integrated spectra (over the radial range indicated in the title of each panel) of $H^{13}CO^+$ $J = 1 - 0$. The spectrum at each spatial location of the data cube was shifted to the systemic velocity prior to integration. The shaded region corresponds to the 1σ error.

Appendix C
Azimuthally Averaged Spectra

Figure 16 shows the azimuthally averaged spectra of HCO^+ and $H^{13}CO^+$ $J = 1 - 0$, together with model spectra from the MCMC fits.

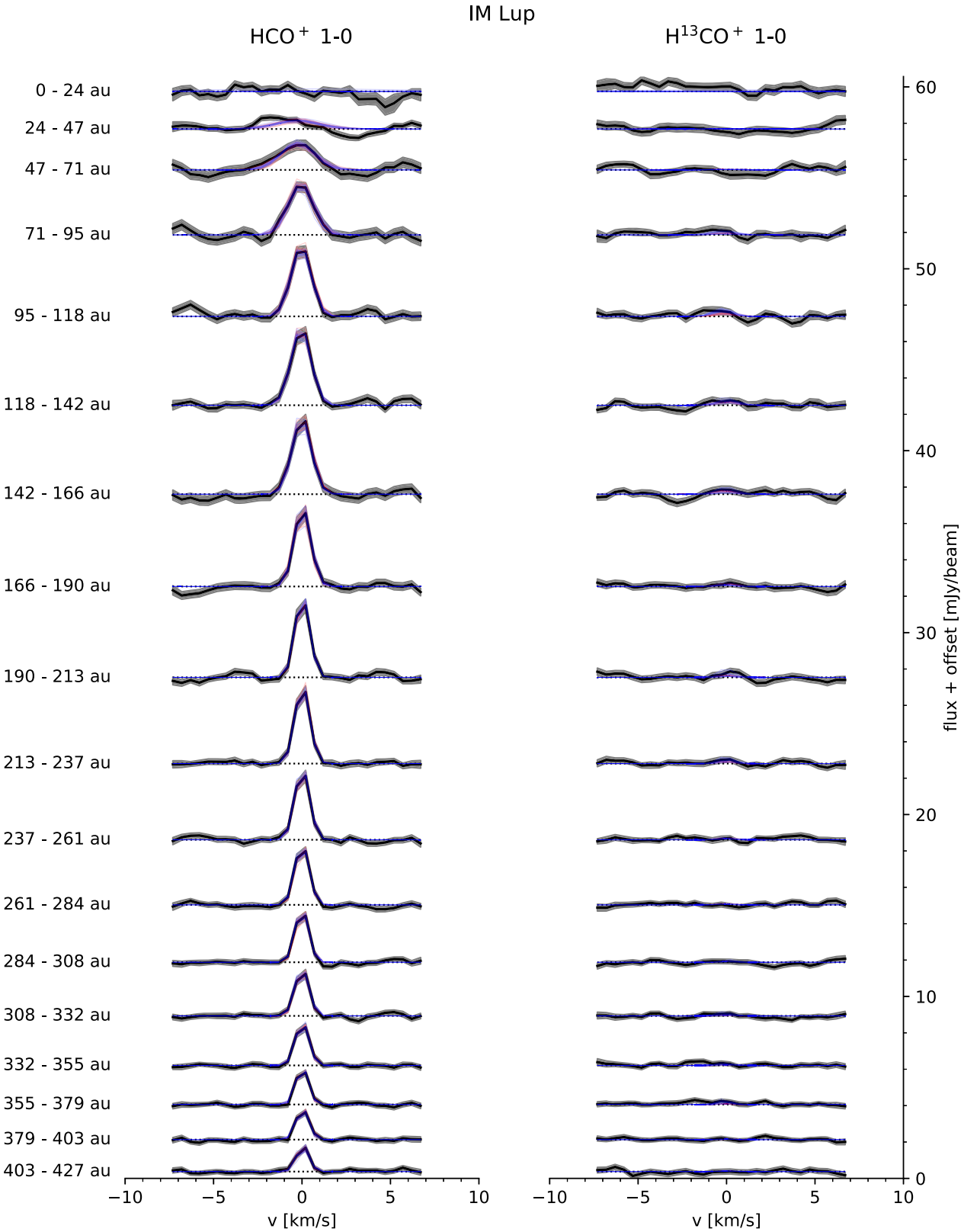

Figure 16. The black curves show azimuthally averaged spectra for IM Lup. Spectra are vertically offset for clarity. The shaded region marks the 1σ error. The horizontal dotted line marks the zero flux level. For each spectrum, we show 20 randomly selected model spectra from the MCMC with the blue curves ($T_{\rm ex}$ as free parameter) and the red curves ($T_{\rm ex}$ fixed to 30 K). The selection probability of each model was set proportional to its posterior probability. Most of the time, the model spectra overlap closely, so that only the blue curves are visible.

(The complete figure set (7 images) is available.)

Appendix D
Dependence of HCO^+ Column Density on Assumed Excitation Temperature

In our fiducial fits, the excitation temperature is a free parameter. In order to explore the dependence of our results on the excitation temperature, we performed additional fits where the excitation temperature is fixed to 30 K. Figure 17 displays a comparison of the column density profiles derived from the different fits. The comparison is discussed in Section 3.2. Figure 18 shows the optical depth profiles derived assuming $T_{ex} = 30$ K.

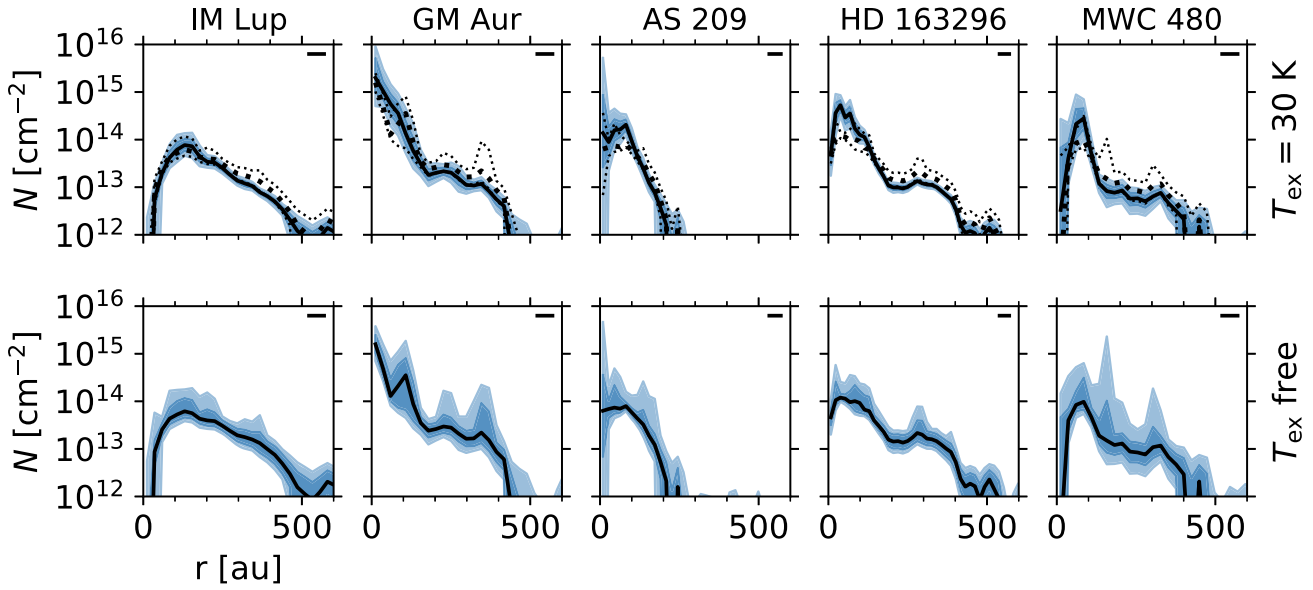

Figure 17. The column density of HCO^+ assuming an excitation temperature of 30 K (top row) and for our fiducial fits where T_{ex} is a free parameter (bottom row). The black solid lines mark the median, while the shading encompasses the regions from the 16th to 84th percentile and from the 2.3th to 97.7th percentile, respectively. To ease comparison, in the top panel, the thick and thin black dotted lines mark the median and the 16th and 84th percentiles of the fits where T_{ex} is a free parameter.

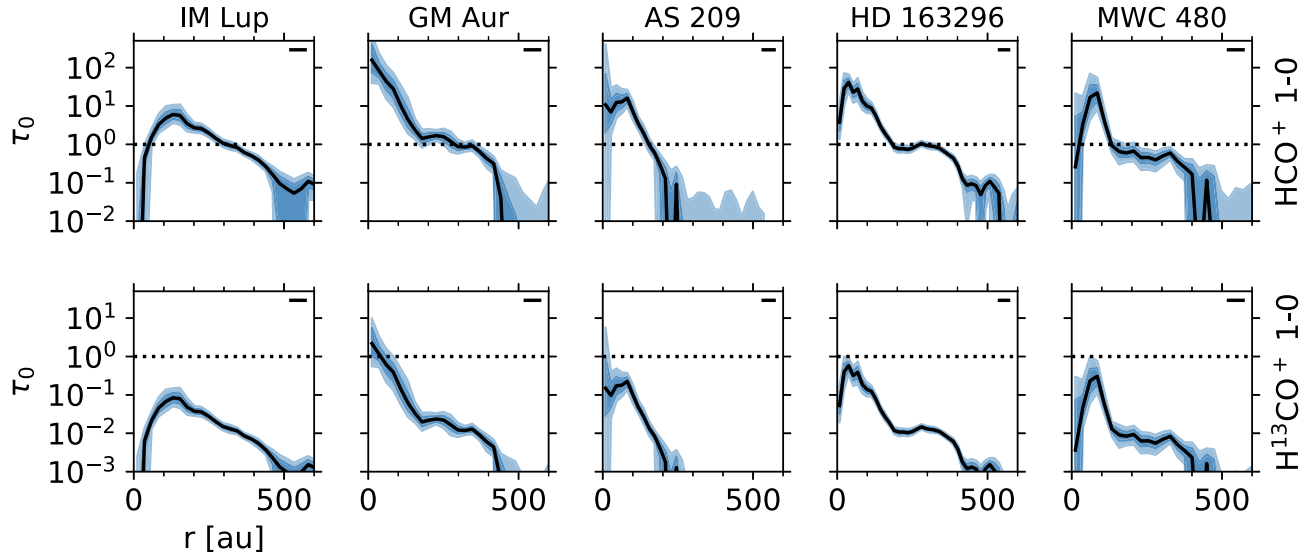

Figure 18. Optical depth profiles of HCO^+ ($J = 1 - 0$) and $H^{13}CO^+$ ($J = 1 - 0$) derived from fitting azimuthally averaged spectra assuming $T_{ex} = 30$ K. The black lines mark the median, while the shading encompasses the regions from the 16th to 84th percentile and from the 2.3th to 97.7th percentile, respectively.

Appendix E
Template Disk Chemistry Models

The top panels in Figure 19 show the 2D (R, Z) distributions of the number of hydrogen nuclei and gas temperature in the template disk model. The panels in the second row show the abundances of gaseous CO, HCO^+, and electrons relative to hydrogen nuclei in the fiducial model. The panels in the third and fourth rows are for the high-C/O model and the low-ζ model, respectively.

Figure 20 shows the absolute abundances (i.e., number density) of HCO^+ (top row), N_2H^+ (second row), N_2D^+ (third row), and H_3^+ and its deuterated isotopomers (fourth row) in the fiducial model (left), the high-C/O model (middle), and the low-ζ model (right).

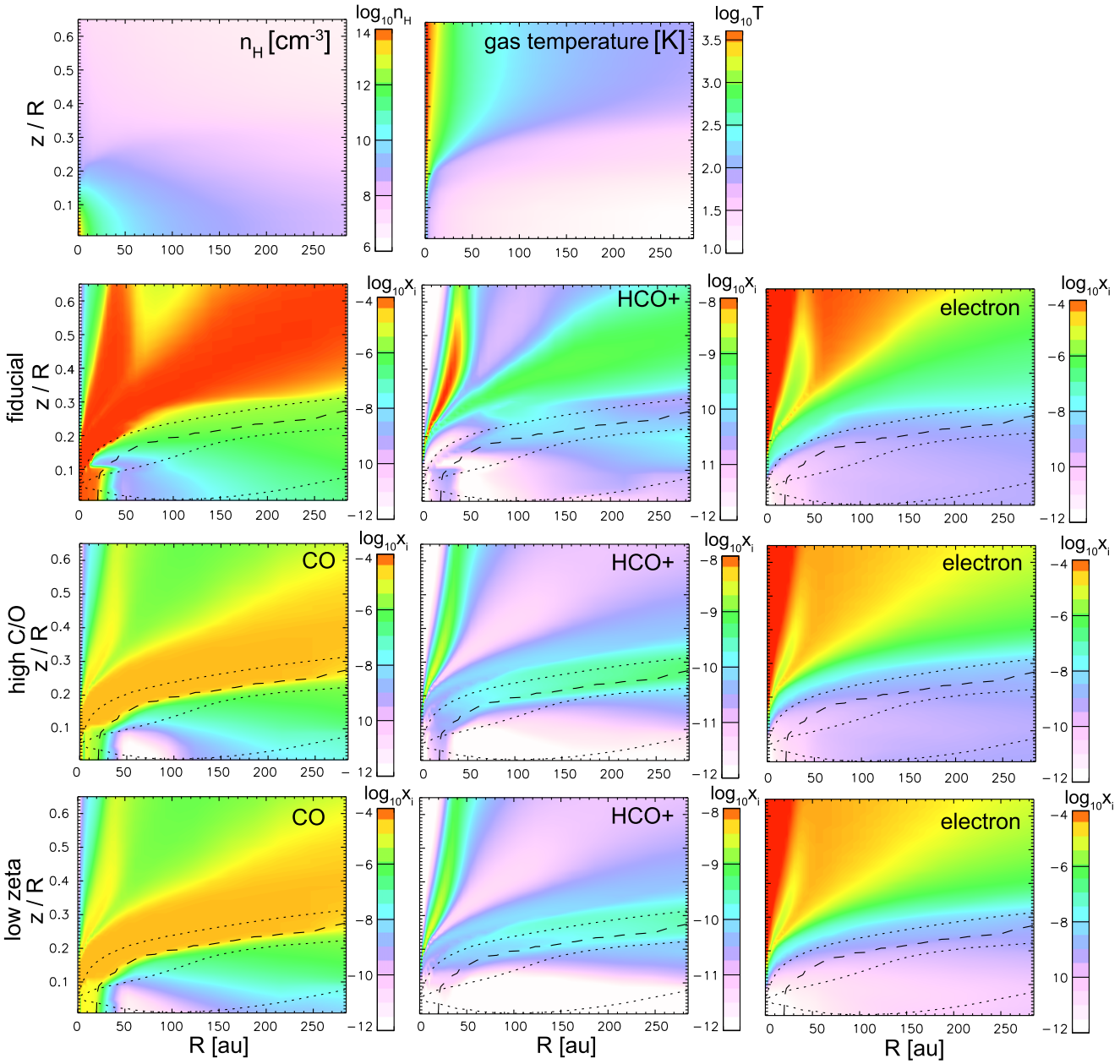

Figure 19. Number density of hydrogen nuclei (n_H) and gas temperature of the template disk model are shown in the top row. Furthermore, we show the abundances of CO (left column), HCO^+ (middle column), and electrons (right column) relative to hydrogen nuclei in the fiducial model (second row), the CO-depleted model (third row), and the model without CR ionization (low-ζ model; bottom row).

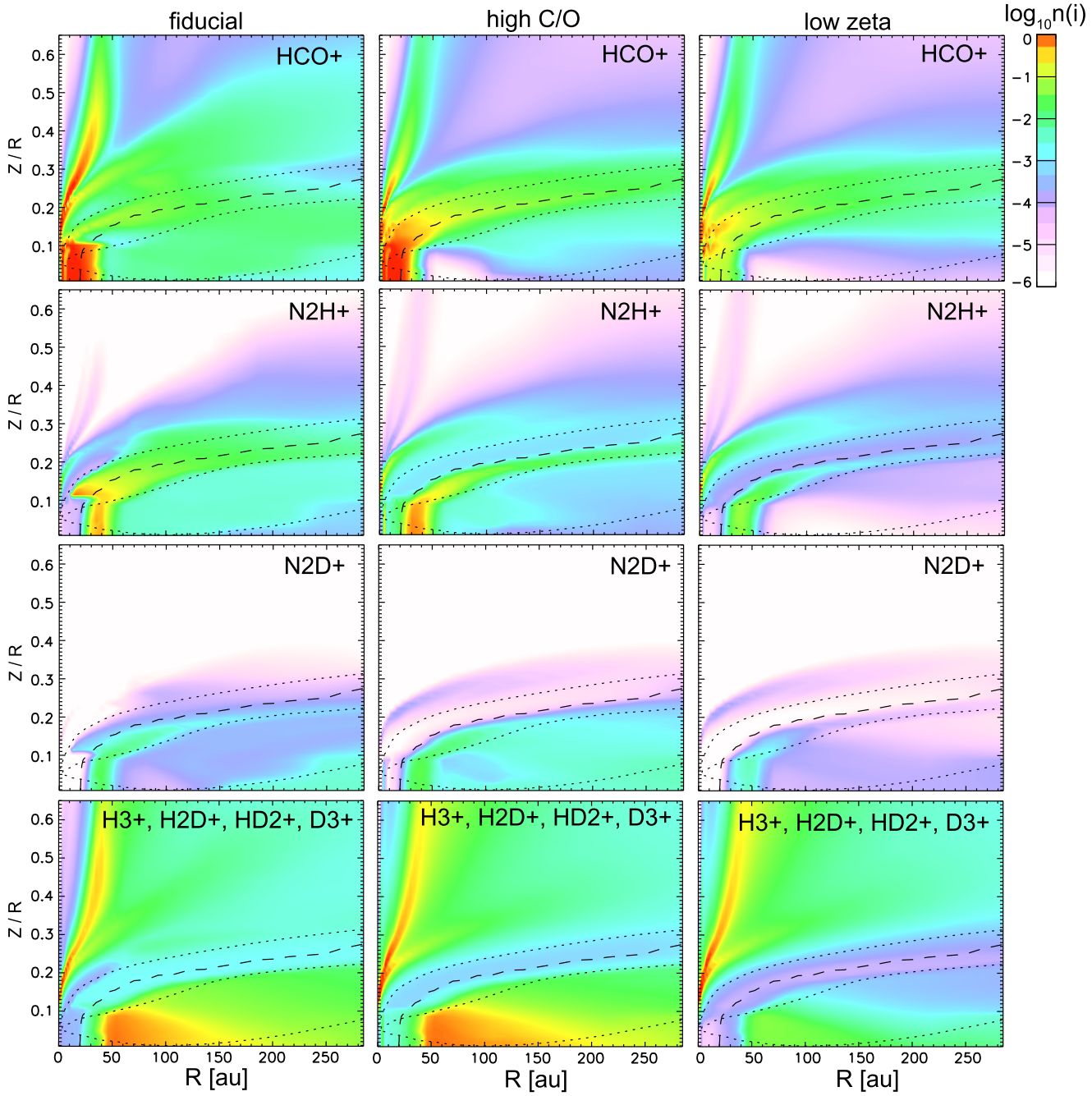

Figure 20. Absolute abundance (i.e., number density in units of cm^{-3}) of major molecular ions in the fiducial disk model (left column), high-C/O model (middle column), and low-ζ model (right column).

ORCID iDs

Yuri Aikawa https://orcid.org/0000-0003-3283-6884
Gianni Cataldi https://orcid.org/0000-0002-2700-9676
Yoshihide Yamato https://orcid.org/0000-0003-4099-6941
Ke Zhang https://orcid.org/0000-0002-0661-7517
Alice S. Booth https://orcid.org/0000-0003-2014-2121
Kenji Furuya https://orcid.org/0000-0002-2026-8157
Sean M. Andrews https://orcid.org/0000-0003-2253-2270
Jaehan Bae https://orcid.org/0000-0001-7258-770X
Edwin A. Bergin https://orcid.org/0000-0003-4179-6394
Jennifer B. Bergner https://orcid.org/0000-0002-8716-0482
Arthur D. Bosman https://orcid.org/0000-0003-4001-3589
L. Ilsedore Cleeves https://orcid.org/0000-0003-2076-8001
Ian Czekala https://orcid.org/0000-0002-1483-8811
Viviana V. Guzmán https://orcid.org/0000-0003-4784-3040
Jane Huang https://orcid.org/0000-0001-6947-6072
John D. Ilee https://orcid.org/0000-0003-1008-1142
Charles J. Law https://orcid.org/0000-0003-1413-1776
Romane Le Gal https://orcid.org/0000-0003-1837-3772
Ryan A. Loomis https://orcid.org/0000-0002-8932-1219
François Ménard https://orcid.org/0000-0002-1637-7393
Hideko Nomura https://orcid.org/0000-0002-7058-7682
Karin I. Öberg https://orcid.org/0000-0001-8798-1347
Chunhua Qi https://orcid.org/0000-0001-8642-1786
Kamber R. Schwarz https://orcid.org/0000-0002-6429-9457
Richard Teague https://orcid.org/0000-0003-1534-5186

Takashi Tsukagoshi https://orcid.org/0000-0002-6034-2892
Catherine Walsh https://orcid.org/0000-0001-6078-786X
David J. Wilner https://orcid.org/0000-0003-1526-7587

References

Aikawa, Y., Furuya, K., Hincelin, U., & Herbst, E. 2018, ApJ, 855, 119
Aikawa, Y., Furuya, K., Nomura, H., & Qi, C. 2015, ApJ, 807, 120
Aikawa, Y., & Herbst, E. 2001, A&A, 371, 1107
Aikawa, Y., Miyama, S. M., Nakano, T., & Umebayashi, T. 1996, ApJ, 467, 684
Aikawa, Y., & Nomura, H. 2006, ApJ, 642, 1152
Alarcón, F., Bosman, A. D., Bergin, E. A., et al. 2021, ApJS, 257, 8
Andrews, S. M., Huang, J., Pérez, L. M., et al. 2018, ApJL, 869, L41
Astropy Collaboration, Robitaille, T. P., Tollerud, E. J., et al. 2013, A&A, 558, A33
Bai, X.-N., & Stone, J. M. 2013, ApJ, 769, 76
Bergin, E. A., Aikawa, Y., Blake, G. A., & van Dishoeck, E. F. 2007, in Protostars and Planets V, ed. B. Reipurth, D. Jewitt, & K. Keil (Tucson, AZ: Univ. Arizona Press), 751
Bergin, E. A., Cleeves, L. I., Crockett, N., & Blake, G. A. 2014, FaDi, 168, 61
Bergin, E. A., Du, F., Cleeves, L. I., et al. 2016, ApJ, 831, 101
Béthune, W., Lesur, G., & Ferreira, J. 2017, A&A, 600, A75
Bosman, A. D., Alarcón, F., Bergin, E. A., et al. 2021, ApJS, 257, 7
Bosman, A. D., Walsh, C., & van Dishoeck, E. F. 2018, A&A, 618, A182
Caselli, P., Walmsley, C. M., Zucconi, A., et al. 2002, ApJ, 565, 344
Cataldi, G., Yamato, Y., Aikawa, Y, et al. 2021, ApJS, 257, 10
Chapillon, E., Parise, B., Guilloteau, S., & Du, F. 2011, A&A, 533, A143
Cieza, L. A., González-Ruilova, C., Hales, A. S., et al. 2021, MNRAS, 501, 2934
Cleeves, L. I., Bergin, E. A., & Adams, F. C. 2014, ApJ, 794, 123
Cleeves, L. I., Bergin, E. A., Qi, C., Adams, F. C., & Öberg, K. I. 2015, ApJ, 799, 204
Czekala, I., Loomis, R. A., Teague, R., et al. 2021, ApJS, 257, 2
Dalgarno, A. 2006, PNAS, 103, 12269
Dionatos, O., Woitke, P., Güdel, M., et al. 2019, A&A, 625, A66
Duley, W. W., & Williams, W. A. 1984, Interstellar Chemistry (London: Academic)
Endres, C. P., Schlemmer, S., Schilke, P., Stutzki, J., & Müller, H. S. P. 2016, JMoSp, 327, 95
Favre, C., Fedele, D., Maud, L., et al. 2019, ApJ, 871, 107
Fedele, D., Tazzari, M., Booth, R., et al. 2018, A&A, 610, A24
Flaherty, K. M., Hughes, A. M., Rose, S. C., et al. 2017, ApJ, 843, 150
Foreman-Mackey, D., Hogg, D. W., Lang, D., & Goodman, J. 2013, PASP, 125, 306
Fujimoto, Y., Krumholz, M. R., & Tachibana, S. 2018, MNRAS, 480, 4025
Furuya, K., & Aikawa, Y. 2014, ApJ, 790, 97
Glassgold, A. E., Najita, J., & Igea, J. 1997, ApJ, 480, 344
Huang, J., Andrews, S. M., Dullemond, C. P., et al. 2018, ApJL, 869, L42
Hunter, J. D. 2007, CSE, 9, 90
Jonkheid, B., Dullemond, C. P., Hogerheijde, M. R., & van Dishoeck, E. F. 2007, A&A, 463, 203
Kama, M., Bruderer, S., van Dishoeck, E. F., et al. 2016, A&A, 592, A83
Krijt, S., Schwarz, K. R., Bergin, E. A., & Ciesla, F. J. 2018, ApJ, 864, 78
Law, C. J., Loomis, R. A., Teague, R., et al. 2021a, ApJS, 257, 3
Law, C. J., Teague, R., Loomis, R. A., et al. 2021b, ApJS, 257, 4
Liu, Y., Dipierro, G., Ragusa, E., et al. 2019, A&A, 622, A75
Long, F., Pinilla, P., Herczeg, G. J., et al. 2018, ApJ, 869, 17
Loomis, R. A., Öberg, K. I., Andrews, S. M., et al. 2018, AJ, 155, 182
Matrà, L., MacGregor, M. A., Kalas, P., et al. 2017, ApJ, 842, 9
McMullin, J. P., Waters, B., Schiebel, D., Young, W., & Golap, K. 2007, in ASP Conf. Ser. 376, Astronomical Data Analysis Software and Systems XVI, ed. R. A. Shaw, F. Hill, & D. J. Bell (San Francisco, CA: ASP), 127
Milam, S. N., Savage, C., Brewster, M. A., Ziurys, L. M., & Wyckoff, S. 2005, ApJ, 634, 1126
Müller, H. S. P., Thorwirth, S., Roth, D. A., & Winnewisser, G. 2001, A&A, 370, L49
Öberg, K. I., Guzmán, V. V., Walsh, C., et al. 2021, ApJS, 257, 1
Öberg, K. I., Qi, C., Fogel, J. K. J., et al. 2011a, ApJ, 734, 98
Öberg, K. I., Qi, C., Wilner, D. J., & Andrews, S. M. 2011b, ApJ, 743, 152
Padovani, M., Ivlev, A. V., Galli, D., & Caselli, P. 2018, A&A, 614, A111
Price-Whelan, A. M., Sipőcz, B. M., Günther, H. M., et al. 2018, AJ, 156, 123
Qi, C., Öberg, K. I., Espaillat, C. C., et al. 2019, ApJ, 882, 160
Qi, C., Öberg, K. I., & Wilner, D. J. 2013a, ApJ, 765, 34
Qi, C., Öberg, K. I., Wilner, D. J., et al. 2013b, Sci, 341, 630
Rab, C., Güdel, M., Padovani, M., et al. 2017, A&A, 603, A96
Rab, C., Güdel, M., Woitke, P., et al. 2018, A&A, 609, A91
Schwarz, K. R., Bergin, E. A., Cleeves, L. I., et al. 2018, ApJ, 856, 85
Sierra, A., Pérez, L. M., Zhang, K., et al. 2021, ApJS, 257, 14
Smirnov-Pinchukov, G. V., Semenov, D. A., Akimkin, V. V., & Henning, T. 2020, A&A, 644, A4
Suzuki, T. K., & Inutsuka, S.-i. 2009, ApJL, 691, L49
Teague, R. 2019, JOSS, 4, 1632
Teague, R., Bae, J., Bergin, E. A., Birnstiel, T., & Foreman-Mackey, D. 2018a, ApJL, 860, L12
Teague, R., Bae, J., Birnstiel, T., & Bergin, E. A. 2018b, ApJ, 868, 113
Teague, R., & Foreman-Mackey, D. 2018, RNAAS, 2, 173
Teague, R., Guilloteau, S., Semenov, D., et al. 2016, A&A, 592, A49
Teague, R., Semenov, D., Guilloteau, S., et al. 2015, A&A, 574, A137
Umebayashi, T., & Nakano, T. 1981, PASJ, 33, 617
Umebayashi, T., & Nakano, T. 1988, PThPS, 96, 151
Umebayashi, T., & Nakano, T. 2009, ApJ, 690, 69
van der Walt, S., Colbert, S. C., & Varoquaux, G. 2011, CSE, 13, 22
Virtanen, P., Gommers, R., Oliphant, T. E., et al. 2020, NatMe, 17, 261
Wakelam, V., Chapillon, E., Dutrey, A., et al. 2019, MNRAS, 484, 1563
Willacy, K. 2007, ApJ, 660, 441
Wilson, T. L. 1999, RPPh, 62, 143
Yen, H.-W., Koch, P. M., Liu, H. B., et al. 2016, ApJ, 832, 204
Zhang, K., Booth, A. S., Law, C. J., et al. 2021, ApJS, 257, 5